Hellenic Arc tsunami generation from M_W8+ 3D margin-wide dynamic rupture earthquake scenarios

Sara Aniko Wirp[1,2], Fabian Kutschera[3], Alice-Agnes Gabriel[3,1], Thomas Ulrich[1], Michael Bader[4], Stefano Lorito[5]

[1]Institute of Geophysics, Department of Earth and Environmental Sciences, Ludwig-Maximilians-University, Munich, Germany
[2]GEOMAR Helmholtz Centre for Ocean Research, Kiel, Germany
[3]Institute of Geophysics and Planetary Physics, Scripps Institution of Oceanography, UC San Diego, California, USA
[4]School of Information, Computation and Technology, Technical University of Munich, Garching, Germany
[5]Istituto Nazionale di Geofisica e Vulcanologia, INGV, Roma, Italy

Key Points:

- We present the first fully-coupled 3D earthquake-tsunami model for the Hellenic Arc megathrust.
- Off-fault plastic deformation reduces shallow slip but enhances vertical seafloor displacement, leading to ∼50 % higher tsunami amplitudes.
- The fully-coupled model reveals complex wave conversion, directivity and dispersion effects, including large acoustic wave amplitudes.

Corresponding author: Alice-Agnes Gabriel, `algabriel@ucsd.edu`

Abstract

The Hellenic Arc subduction zone is the most seismically active region in the Mediterranean, capable of generating large earthquakes and tsunami. Given the proximity of densely populated coastlines, understanding the characteristics of potential future large tsunamigenic earthquakes is crucial for assessing tsunami hazard. We present non-linear shallow water tsunami simulations sourced from the static seafloor displacements of five M_W 8–9 dynamic rupture earthquake scenarios along the Hellenic Arc, varying in hypocentral location, rupture extent, and moment magnitude. In three of these 3D rupture models, slip penetrates the shallow slip-strengthening region of the megathrust, generating uplift patterns modulated by the location of the hypocenter. Our results show that shallow slip and off-fault plastic deformation control the vertical near-trench uplift and tsunami height in the near-field. Maximum tsunami amplitudes reach up to ∼6.6 m near central and eastern Mediterranean coastlines, while the northern Aegean and the western Mediterranean remain mostly shielded by landmasses in all scenarios. One scenario is further extended into a large-scale fully-coupled 3D earthquake-tsunami model, capturing dynamic rupture, seismic and acoustic wave propagation, and time-dependent tsunami generation. The fully-coupled simulation reveals complex interactions between acoustic and tsunami waves during the early generation phase, including dispersion and wave conversions between seismic and ocean acoustic waves not captured by static or linked models. These results highlight the value of integrating 3D dynamic rupture modeling with tsunami simulations, enhance our understanding of tsunami generation mechanisms, and can provide physics-based insights to tsunami hazard assessment and early warning strategies.

Plain Language Summary

The region around the Greek islands is the most earthquake and tsunami-prone area in the Mediterranean. Historically, this region produced powerful earthquakes that triggered tsunami waves, affecting populated coastal areas and devastating towns. Thus, it is important to consider different earthquakes and the tsunamis they generate to better constrain seismic and tsunami hazard. We here use computer models to simulate tsunamis of five possible earthquakes. We vary the earthquake's starting point and get earthquakes of a moment magnitude of 9, which spread across the entire region. The earthquakes produce different vertical deformation patterns, which lead to different ocean wave heights and arrivals on the coasts. The waves reach the coasts around the eastern Mediterranean, but do not extend to France, Spain, or Algeria in the West, as they are protected by land masses. When including plastically deforming rocks in our earthquake models, the tsunami amplitudes get much higher (6.6 m). This study also includes a detailed simulation that combines the earthquake and tsunami in one 3-dimensional model and demonstrates the complexities of tsunami generation. Our results highlight that combined earthquake-tsunami modeling is a powerful tool to improve hazard assessment for this region and elsewhere.

1 Introduction

1.1 The tectonic setting of the Hellenic Arc Subduction Zone

At the Hellenic Arc Subduction Zone (HASZ), the African plate subducts beneath the Eurasian plate at a convergence rate of 25–60 mm/yr (Taymaz et al., 1990; McClusky et al., 2000; Reilinger et al., 2006). This leads to thrust faulting along the outer Hellenic Arc (McKenzie, 1972, 1978; Benetatos et al., 2004). The subduction is suggested to be driven by slab roll-back of the subducting Nubian plate, pushing the African plate towards the Aegean Sea plate (Bohnhoff et al., 2005; Sachpazi et al., 2016; Meng et al., 2021). The resulting arc-orthogonal compression in the west and arc-oblique convergence in the east shape the Hellenic Arc into an elliptical structure (see Fig. 1, a). The interplay of subduction and regional tectonics generates complex deformation patterns, including east-west extension in the inner arc (McClusky et al., 2003; Kreemer & Chamot-Rooke, 2004) and north-south extension in the southern and central Aegean (Kiratzi & Papazachos, 1995; McKenzie, 1978; Pichon & Angelier, 1979). This leads to diverse faulting styles including strike-slip faulting southeast of Crete, associated with the Plini and Strabo trench (Jongsma, 1977), and a transition to more oblique faulting towards the north-west (Goldsworthy et al., 2002; Karakostas & Papadimitriou, 2010; Bie et al., 2017; Chousianitis & Konca, 2019; Cirella et al., 2020), occasionally causing moderate tsunami. Although the HASZ has long been considered to accommodate slip aseismically due to its relatively low seismicity compared to its high convergence rate (e.g., C. B. Papazachos & Kiratzi, 1996; Shaw et al., 2008), recent studies indicate that the megathrust may be fully seismically coupled and capable of generating large earthquakes (Laigle et al., 2004; Ganas & Parsons, 2009), motivating an improved understanding of the characteristics of potential future large tsunami, specifically in the proximity of densely populated coastlines.

1.2 Hellenic Arc tsunamigenic earthquakes

Earthquakes associated with the subducting Hellenic Arc megathrust or surrounding tectonic features, such as splay faults branching off the megathrust, reportedly produced several tsunami (e.g., Galanopoulos, 1960; N. N. Ambraseys, 1962; Antonopoulos, 1980; G. Papadopoulos & Chalkis, 1984; Guidoboni & Comastri, 1997; G. Papadopoulos et al., 2012). The largest known earthquakes of the HASZ are the AD 365 and the 1303 Crete events, which ruptured the south-western and eastern segment of the Hellenic Arc, generating estimated moment magnitudes of $M_W \approx 8$ (see Fig. 1, b) (N. N. Ambraseys, 1994; Guidoboni et al., 1994; El-Sayed et al., 2000; Hamouda, 2006; Shaw, 2012; E. E. Papadimitriou & Karakostas, 2008). Both earthquakes sourced devastating tsunamis that inundated many coastal regions of the eastern Mediterranean, causing destruction and loss of life (G. A. Papadopoulos et al., 2014; Cirella et al., 2020).

Several moderate earthquakes with moment magnitudes ranging from $M_W \sim 5.5$–6.8 (in 1494, 1612, 1741, 2000, 2009, 2017, 2018, and 2020) produced smaller and more localized tsunami (G. A. Papadopoulos et al., 2010; Bocchini et al., 2020a; Baglione et al., 2021; Mohammad & Riadi, 2021). The 1st July 2009 event, for example, ruptured the offshore margin near the trench of the HASZ south of Crete, probably breaking a reverse fault of the upper plate and causing a tsunami height of 0.3 m. The $M_W 6.8$ 25th October 2018 event that occurred near Zakynthos island was followed by a moderate tsunami recorded by several tide-gauge stations in the Ionian Sea (Cirella et al., 2020; G. A. Papadopoulos, Agalos, et al., 2020). Two $M_W 6.6$ thrust-faulting events occurred in May 2020 near the location of the 2009 $M_W 6.4$ earthquake, south of Crete, and both caused tsunami reaching the Crete coast (e.g., G. A. Papadopoulos, Lekkas, et al., 2020). Other thrust-faulting interplate events, such as the 1952 $M_W 7.0$ and the 1972 $M_W 6.5$ earthquakes south of Crete (N. Papadopoulos & Chatziathanasiou, 2011), or the 2013 $M_W \sim 6.6$

earthquake of the western HASZ (Vallianatos et al., 2014) did not cause any noticeable tsunami.

The earthquake and tsunami history of the HASZ makes it the most seismically active tsunami-prone region of the Mediterranean Sea (Pirazzoli et al., 1996; Vannucci et al., 2004; Ganas & Parsons, 2009; Ozer et al., 2018; Chorozoglou & Papadimitriou, 2019). Several $M_W \geq 7$ earthquakes related to the HASZ (B. Papazachos & Papazachou, 2003; Guidoboni et al., 2005; N. Ambraseys, 2009), including 11 earthquakes of moment magnitude ≥ 7 have been recorded since 1900 (E. Papadimitriou et al., 2016), motivating the focus of this study on large tsunamigenic earthquake scenarios. Probabilistic seismic and tsunami hazard studies agree on the high hazard posed by the HASZ (e.g., Coban & Sayil, 2020; G. A. Papadopoulos & Kijko, 1991), associated with its active tectonics. In particular, Probabilistic tsunami hazard assessment (PTHA) studies (Sørensen et al., 2012) confirm that the eastern Mediterranean is under the highest tsunami hazard within the Mediterranean Sea.

1.3 Earthquake sources in tsunami models

Tsunami models, particularly for PTHA studies, commonly use simplified static or kinematic earthquake source models. These models may utilize different representations of complexities in their initial conditions, such as depth-dependent structural properties (Scala et al., 2020; Basili et al., 2021) or stochastically distributed heterogeneous slip (Small & Melgar, 2021; Cifuentes-Lobos et al., 2023). Also, different filters can be considered when linking earthquake sources to tsunami (Madden et al., 2020; K. Sementsov & Nosov, 2023; Abbate et al., 2024; Scala et al., 2024; K. A. Sementsov et al., 2024). Testing of stochastic earthquake models against deep ocean observations shows that the tsunami they generate are statistically similar to the observations themselves, at least in the deep sea and in the far-field (Davies, 2019). It remains to be further assessed whether these models are equally performing in the near-field and in terms of coastal inundation, as well as if the degree of variability typically imparted to these models can be reduced. Several solutions have been proposed in this respect, either based on statistical or machine-learning approaches (Lorito et al., 2015; Volpe et al., 2019; Davies et al., 2022; Briseid Storrøsten et al., 2024; Abbate et al., 2025).

Stochastic earthquake models may not realistically represent the highly complex physical and time-dependent rupture dynamics of natural earthquakes (E. Tinti et al., 2021), that include, for example, rupture complexity, interactions with off-fault plastic deformation, supershear, slow rupture speeds, or near-surface rake rotation (Geist, 2002; Ma & Nie, 2019; Wirp et al., 2021; Elbanna et al., 2021; Ulrich et al., 2022; Kutschera, Gabriel, et al., 2024). The instantaneous uniform slip derived from point-source seismic inversion and/or scaling relations (e.g., Maeda et al., 2013; Melgar & Bock, 2013; Dias et al., 2014; Mori et al., 2017; Davies et al., 2018; Davies, 2019; Gibbons et al., 2022), can differ significantly from the complex spatio-temporal varying seafloor displacements generated by dynamic rupture simulations (Wendt et al., 2009; Madden et al., 2020). A time-dependent tsunami source initialization can specifically make a difference for long rupture duration earthquakes, large and/or slow earthquakes (Luo & Liu, 2021; Scala et al., 2024; K. A. Sementsov et al., 2024).

Dynamic rupture models may complement simpler tsunami hazard approaches and help better understand the physics underlying the propagation of earthquake rupture, reduce nonphysical variability, and unravel how ground velocities and acceleration depend on complex earthquake dynamics (Dunham & Archuleta, 2005; Ripperger et al., 2008; Z. Shi & Day, 2013; Galvez et al., 2016; Withers et al., 2018; Gallovič & Valentová, 2023). Despite challenges in constraining dynamic input parameters such as the pre-stress distribution (Lambert et al., 2021; Tang et al., 2021; Chen et al., 2024), dynamic rupture models are physically self-consistent and can be used to directly source a tsunami simulation. Various approaches exist to link dynamic rupture to tsunami modeling. One possibility is to extract the static or time-dependent seafloor displacement from a dynamic rupture simulation and use it as static or time-dependent input for a tsunami simulation (Wendt et al., 2009; Saito et al., 2019; Madden et al., 2020; Wirp et al., 2021; Prada et al., 2021; Wilson & Ma, 2021; Ma, 2022; Ulrich et al., 2022; Kutschera, Gabriel, et al., 2024).

"Fully-coupled" earthquake-tsunami models contain a water layer atop a dynamic rupture earthquake model and can account for the non-hydrostatic ocean response (Lotto & Dunham, 2015; Lotto et al., 2018; Krenz et al., 2021; Wilson & Ma, 2021; Ma, 2022). Such models simultaneously solve for the rupture process, seismic wave propagation in elastic media and acoustic wave propagation in the ocean, and the induced tsunami, while capturing dispersion effects during the tsunami generation phase (Krenz et al., 2021; Abrahams et al., 2023; Kutschera, Gabriel, et al., 2024), where the tsunami is modeled through a gravity-restoring boundary condition at the sea surface (Sec. 2.3).

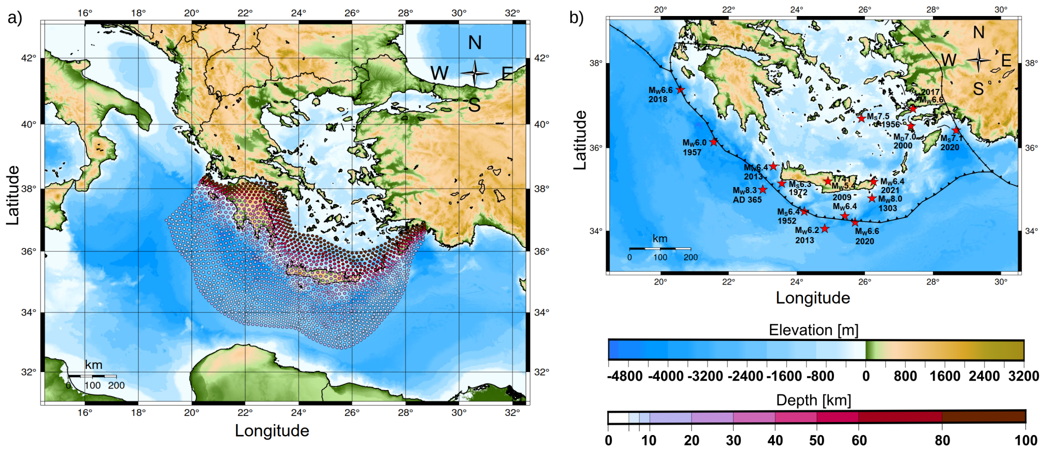

Figure 1. Dynamic rupture modeling domain: a) The Hellenic Arc megathrust by Scala et al. (2020); Basili et al. (2021) used in this study. The dark red color indicates deeper fault depths. Note that the tsunami modeling computational domain extends beyond the dynamic rupture modeling domain (Figs. 3 and 4). b) Zoom into the Hellenic Arc region with M_W >5.4 earthquakes (red stars) related to the Hellenic Arc subduction or surrounding tectonics (G. A. Papadopoulos et al., 2010; Bocchini et al., 2020b; Cirella et al., 2020; Coban & Sayil, 2020). Plate boundaries are indicated by black lines (Bird, 2003), and the convergent subduction margin is marked with triangles.

1.4 Overview of this study

In this study, we investigate the dynamics of large tsunami sourced by M_W 8–9 megathrust earthquakes across the HASZ using two techniques to model earthquake-tsunami interactions, one-way linked models using the seafloor displacement from 3D dynamic rupture simulations and a fully-coupled simulation (Abrahams et al., 2023).

We use five recently developed physics-based dynamic rupture models, named HE, HM, HW, HEP, and HEA following (Wirp et al., 2024), that capture a range of plausible rupture scenarios, detailed hereinafter (Sec. 2). The models differ in epicentral locations, rupture extent, and magnitude, resulting in variations of shallow slip amplification and co-seismic uplift. The hypocenter of model HE is prescribed below southeast

Crete at a depth of 30 km (Fig. 2a,f). We vary the hypocentral location to investigate the effect of rupture propagation direction and slip distribution on co-seismic seafloor displacements and tsunami propagation. In model HM (middle hypocenter, Fig. 2b,g), the hypocenter is located between Crete and Peloponnese. In model HW (western hypocenter, Fig. 2c,h), it is located further west, below northwest Greece. Both models have the same hypocentral depth as model HE. Model HEP includes a non-associative (visco-)plastic Drucker-Prager rheology (Andrews, 2005; Wollherr et al., 2018) to analyze the effects of weak sediments on co-seismic seafloor deformation and tsunami amplitudes. In model HEA, we use a single prestress asperity to limit the potential rupture size by reducing the initial loading outside this region, resulting in an M_W ∼8 event.

We remodel the selected scenarios at higher resolution to use the same computational mesh for both the fully-coupled scenario and the linked earthquake-tsunami models. We select three margin-wide rupture models (HE, HM, HW) that vary in hypocentral location, shallow fault slip, and consequent evolving seafloor displacement. Additionally, we use an earthquake rupture scenario that includes off-fault plastic yielding (HEP), leading to a much higher seafloor displacement than the other models. Lastly, we use a single initial stress asperity model (HEA) at the approximate location of the 1303 Crete earthquake (Wirp et al., 2024).

The dynamic rupture and tsunami setups are detailed in Sec. 2, while Sec. 3.1 summarizes the results of the five earthquake rupture scenarios used for this study. Sec. 3.1.3 highlights the results of the tsunami sourced by the static seafloor displacement of the dynamic rupture simulations. We show "worst-case" scenarios in terms of earthquake magnitude and their earthquake-tsunami interaction simulated in the HASZ. We investigate how adding off-fault plastic yielding or a stress asperity in the dynamic rupture model may influence tsunami generation and propagation in this region. We further extend scenario HE into one of the largest-scale fully-coupled 3D earthquake-tsunami models to date, to better understand tsunami genesis (Sec. 3.2). We discuss the limitations and challenges of both approaches and provide guidance on selecting the appropriate method for different research questions.

2 Methods

This section describes the methods and workflow for performing one-way linked and 3D fully-coupled dynamic rupture earthquake-tsunami models. We first introduce SeisSol, the open-source scientific software for the numerical simulation of seismic wave phenomena and earthquake dynamics (Sec. 2.1), before we clarify differences between the one-way linked shallow water tsunami models simulated with GeoClaw (Sec. 2.2) and the fully-coupled approach implemented in SeisSol (Sec. 2.3). We then detail the model domain (Sec. 2.4), followed by the dynamic rupture modeling setup, which includes on-fault friction and initial stresses (Sec. 2.5), and off-fault plasticity (Sec. 2.6).

2.1 Dynamic rupture modeling with SeisSol

We use the open-source software package SeisSol (`https://seissol.org`; Uphoff et al. (2024)) on the Munich high-performance supercomputing cluster SuperMUC-NG to simulate five 3D earthquake dynamic rupture scenarios on the HASZ. SeisSol uses the Arbitrary high-order accurate DERivative Discontinuous Galerkin method (ADER-DG) (Käser & Dumbser, 2006; Dumbser & Käser, 2006; de la Puente et al., 2009) and achieves high-order accuracy in both space and time in modeling the seismic wavefield (Breuer et al., 2015; Heinecke et al., 2014; Uphoff et al., 2017; Krenz et al., 2021). Here, we simultaneously simulate non-linear frictional on-fault failure, off-fault plastic deformation, and seismic wave propagation. SeisSol accounts for (visco-)plastic Drucker-Prager off-fault plastic deformation (Andrews, 2005; Wollherr et al., 2018). We use unstructured tetrahedral meshes enabling models incorporating complex three-dimensional model geometries and topography (e.g., Ulrich, Gabriel, et al., 2019; Wolf et al., 2020; Li et al., 2023; Taufiqurrahman et al., 2023; Kutschera, Gabriel, et al., 2024). The software has been verified against community benchmarks for dynamic rupture earthquake simulations (Pelties et al., 2014; Harris et al., 2018; Vyas et al., 2023), including heterogeneous off-fault material and initial on-fault stresses.

2.2 One-way linked tsunami modeling with GeoClaw

In the one-way linking approach, we use the static displacement at the end of each dynamic rupture simulation (400 s after rupture onset) to source a state-of-the-art tsunami simulation. By this time, the rupture process has terminated, and the ground deformation pattern is permanent, with no transient waves remaining (Madden et al., 2020). We use the software GeoClaw (Berger et al., 2011; LeVeque & George, 2008; LeVeque et al., 2011), which implements the nonlinear 2-dimensional depth-averaged shallow water equations with adaptive mesh refinement (AMR) using high-resolution finite volume methods. Our GeoClaw simulations do not account for inundation. GeoClaw has been extensively validated (e.g., Arcos & LeVeque, 2015; Omira et al., 2022; Kutschera, Jia, et al., 2024) and approved by the US National Tsunami Hazard Mitigation Program (Gonzalez et al., 2011).

GeoClaw can handle heterogeneous seafloor displacements to source a tsunami. We closely follow Ulrich et al. (2022) to transform the SeisSol surface output to GeoClaw input. To approximate the contribution to tsunami generation of horizontal coseismic displacements, particularly relevant with strong bathymetric gradients, we apply the Tanioka filter (Tanioka & Satake, 1996). The element-wise unstructured triangular seafloor output from SeisSol is stored in a Cartesian coordinate system. This output is interpolated onto a structured latitude–longitude grid on a spherical surface. We apply a Hanning window to prevent sharp displacement discontinuities at the limits of the region of imposed displacements. We use the GEBCO (GEBCO Compilation Group, 2019) bathymetry dataset with a horizontal resolution of 15 arcsec (approx. 380 m). The tsunami model domain extends beyond the earthquake model domain and captures the source region, as well as most of the Mediterranean Sea (Fig. 3), from 30° in longitude from 7° to 37° and 16° in latitude from 30° to 46°. We use three AMR levels in our GeoClaw simulations, with the finest grid spanning 48 arcsec. We simulate tsunami propagation for 8 hours, which is sufficient to capture tsunami extrema everywhere in the modeled domain. Each 8-hour GeoClaw simulation required <6 CPU hours, which is considerably less than the 3D fully coupled simulation described in the next sections.

2.3 3D fully-coupled earthquake-tsunami modeling

We showcase one high-resolution 3D fully-coupled earthquake-tsunami simulation for the HASZ. Fully-coupled earthquake-tsunami models combine earthquake rupture dynamics, wave propagation in elastic and acoustic media, and tsunami propagation in a compressible ocean (Lotto & Dunham, 2015; Lotto et al., 2018; Wilson & Ma, 2021; Ma, 2022) in a self-consistent way. They naturally account for the non-hydrostatic ocean response that leads to dispersion effects during the tsunami generation and propagation phases. At the interface between the acoustic and elastic medium, the physical conditions can be matched numerically, by solving the Riemann problem (Wilcox et al., 2010) exactly and as a combination of both, elastic and acoustic properties. This elastic-acoustic coupling is implemented in SeisSol by treating the acoustic wave equation as a special case of the elastic wave equation (Krenz et al., 2021). In the water layer, the rigidity is set to zero ($\mu = 0$). The acoustic wave speed is set to $\sim$1500 ms^{-1}. Our fully-coupled model accounts for gravitational effects using a modified surface boundary condition, which is applied on the equilibrium ocean surface, to correctly capture the onset of tsunami propagation (Krenz et al., 2021). Aiming at capturing the full physics of the tsunami generation process, we build a structural model including a three-dimensional water layer of variable depth on top of a realistic bathymetric surface representation. For the fully-coupled model, we choose the HE earthquake dynamic rupture scenario. The fully-coupled model and the one-way linked earthquake tsunami scenario share the same initial conditions and the same solid Earth mesh.

2.4 Computational domain and meshing

We use the same HASZ slab geometry as in (Wirp et al., 2024), which is based on tsunami hazard studies of the Mediterranean region (Scala et al., 2020; Basili et al., 2021). The modeling domain of the dynamic rupture model spans most of the Eastern Mediterranean, including southern Italy and parts of Sicily in the West, the African coast of Libya and Egypt in the south, extensive parts of Turkey's East Coast, and the whole Greece up to the Black Sea in the North (see Fig. 1), and reaches the western limit of Cyprus island in the east. The mesh of the dynamic rupture model is generated from the mesh used for the fully-coupled model by excluding the water layer part. It consists of 87.66 million elements. The fault is resolved by a 1000 m mesh. We use basis functions of polynomial order $p = 5$ (i.e., sixth-order accuracy in time and space of the wave propagation kernels), which is sufficiently high to accurately resolve rupture dynamics (Wirp et al., 2024).

In the fully-coupled SeisSol models, to reduce the high computational costs associated with the oceanic acoustic and tsunami wave simulation (see Fig. A1), the water layer of the fully-coupled DR-tsunami model spans not the complete domain but a region of 1.100 by 800 km. Thus, the water layer has a smaller horizontal extent than the modeling domain of the dynamic rupture simulations. It includes large parts of the Greek coast and a part of the Libyan coast in northern Africa (see Figs. A1a,b,c). In the SeisSol mesh, we allow for static coarsening of the mesh elements towards the domain boundaries (Figs. A1a,d).

A finely sampled bathymetry is primordial for being able to model accurately propagation of shorter tsunami wavelengths in shallower water depth regions. The water layer is meshed with a spatial discretization of 200 m, small enough to model wavelengths of ≈1200 m; resulting in a total mesh size of 243 million elements for the fully-coupled model.

Each dynamic rupture earthquake model required ≈8 h on 700 nodes (each with 48 cores) on the Munich supercomputer SuperMUC-NG, which equals to 268,800 core hours. The fully-coupled model is an order more costly and required ≈30 h on 700 nodes, which equals to 1,008,000 core hours. The dynamic rupture models include 6.6 min simulation time, producing an output size of 2.4 TB, while the fully-coupled earthquake-tsunami model captures 5 min simulation time, producing an output of 2.9 TB.

2.5 Initial stresses and fault friction

As in Wirp et al. (2024), we prescribe a non-Andersonian prestress state. We define a homogeneous regional stress field as a Cartesian stress tensor constrained by assumptions on the effective normal stress depth gradient, and seismo-tectonic constraints on stress orientation and stress amplitude ratio.

The stress shape ratio Φ balances the principal stress amplitudes and is defined as (Lund & Townend, 2007):

$$\Phi = \frac{\sigma_2 - \sigma_3}{\sigma_1 - \sigma_3}\,, \tag{1}$$

where σ_i are the principal stresses with σ_1 being the orientation of the maximum compressive principal stress and σ_3 the orientation of the minimum stress. We assume a stress shape ratio of Φ=0.4, consistent with stress inversion results for interplate events around Crete by Bohnhoff et al. (2005). The assumed maximum principal stress σ_1 dips shallowly at 10° at an azimuth of 280° (290° for model HEA), σ_2 is horizontal, and σ_3 steeply plunges and is normal to the σ_1-σ_2 plane.

All five dynamic rupture models use a linear slip-weakening (LSW) friction law (Ida, 1972; Andrews, 1976) and all fault-friction parameters are summarized in Table 1. The seismogenic part of the Hellenic Arc subduction interface has been inferred at depths of 15–45 km (Vernant et al., 2014), while unconsolidated sediments in the upper 15 km may influence shallow rupture behavior and tsunami generation. We use a depth-dependent strength drop by applying varying dynamic friction value $\mu_\mathrm{d} = 1.2$–0.2 and a constant Byerlee compatible static friction value $\mu_\mathrm{s} = 0.6$ (Byerlee & Summers, 1976). In all models expect HEA, the uppermost 15 km of the fault are assumed to be slip-strengthening ($\mu_\mathrm{s} \geq \mu_\mathrm{d}$, and for model HEA in the uppermost 10 km) to capture the aseismic deformation behavior of the upper fault. Slip-weakening frictional behavior is assumed for the depth of 15–43.3 km (10–43.3 km for HEA, respectively), while depths deeper than 43.3 km are governed by slip-strengthening. The critical slip weakening distance D_c is constant and set to 1.0 m in all models.

The relative prestress ratio $\mathcal{R}$ (e.g., Aochi & Madariaga, 2003) is defined as:

$$\mathcal{R} = \frac{\Delta\tau}{\Delta\tau_b} = \frac{\tau - \mu_\mathrm{d}\sigma_n'}{c + (\mu_\mathrm{s} - \mu_\mathrm{d})\sigma_n}, \tag{2}$$

and relates the maximum potential stress-drop during dynamic rupture $\Delta\tau$ to the frictional breakdown strength-drop $\Delta\tau_b$, with c being the frictional cohesion, and μ_d and μ_s the dynamic and static friction coefficients, respectively. We define $\mathcal{R}_0 \geq \mathcal{R}$ as the maximum possible value of $\mathcal{R}$. $\mathcal{R} = \mathcal{R}_0 = 1$ characterizes critically prestressed faults that are also optimally orientated towards the regional prestress tensor. $\mathcal{R}_0$ is set to 0.7, as in (Wirp et al., 2024).

We define the pore fluid pressure ratio as:

$$\sigma_{zz}'(z) = (1 - \gamma)\rho g z \tag{3}$$

with σ_{zz}' being the effective lithostatic stress, γ the pore fluid pressure ratio defined as $\gamma = \rho_{water}/\rho_{rocks}$ which is set to 0.97, g the gravitational force, ρ the density, and z the depth.

2.6 Off-fault plasticity

In all dynamic rupture models, we use the 1D isotropic version of the PREM (Preliminary Reference Earth Model) velocity model (Dziewonski & Anderson, 1981; Bormann, 2009). The HASZ is characterized by unconsolidated weak sediments in the upper 15 kms (Jongsma, 1977; Pichon & Angelier, 1979; Le Pichon & Angelier, 1981; Taymaz et al., 1990; Bohnhoff et al., 2001; Casten & Snopek, 2006; Shaw & Jackson, 2010). One of the five dynamic rupture models (model HEP) allows for off-fault plastic deformation (Wirp et al., 2024), which provides a more realistic representation of weak off-slab sediments co-seismically deforming. We use a non-associative (visco-)plastic Drucker-Prager rheology (Andrews, 2005; Wollherr et al., 2018). As in Ulrich, Gabriel, et al. (2019); Wirp et al. (2024), the bulk cohesion $C(z)$ varies with depth

$$C(z) = C_0 + C_1(z)\sigma_{zz}'. \tag{4}$$

$C_0 = 0.3$ MPa controls the location and amplitude of the off-fault plastic yielding and is constant. $C_1(z)$ defines rock hardening with depth, σ_{zz}' is the effective lithostatic stress. The bulk material's friction coefficient ν, defined in the elastic solid medium, is assumed to be constant and is set to 0.6, equaling the fault static friction coefficient ($\mu_s = 0.6$). The off-fault plastic strain $\eta(t)$ at the end of the simulation time t (Ma, 2008) is quantified as

$$\eta(t) = \int_0^t \sqrt{\frac{1}{2}\dot{\epsilon}_{i,j}^p \dot{\epsilon}_{i,j}^p}\,, \tag{5}$$

Parameter	Margin-wide rupture models
Static friction coefficient (μ_s)	0.6
Dynamic friction coefficient (μ_d, depth-dependent)	1.2-0.3
Critical slip distance (D_c) [m]	1.0
SH_{max} [deg]	280 [a]
slip-weakening depths [km]	15–43.3 [b]
Nucleation depth [km]	∼30 [c]
Maximum relative pre-stress ratio (R_0)	0.7
Pore fluid ratio (γ)	0.97
Stress shape ratio (Φ)	0.4

Table 1. Dynamic rupture parameters for five dynamic rupture models HE, HM, HW, HEP, and HEA, selected from the ensemble in Wirp et al. (2024). [a] The orientation of the maximum horizontal stress is SH_{max} =280 ° for models HE (eastern hypocenter), HM (middle hypocenter), HW (western hypocenter), and HEP (model HE including off-fault plasticity) but SH_{max} =290 ° for HEA (single-asperity model). [b] The seismogenic depth is 15–43.3 km for models HE, HM, HW, and HEP but 10–43.3 km for HEA. [c] The hypocenter depth is ∼30 km for models HE, HM, HW, and HEP but ∼7 km for model HEA.

with $\dot{\epsilon}_{ij}$ being the time-dependent plastic strain increment.

3 Results

3.1 One-way linked dynamic rupture earthquake-tsunami scenarios

3.1.1 Rupture dynamics

In the following, we summarize the rupture dynamics in our selected five scenarios. For more details, the reader is referred to Wirp et al. (2024). The three margin-wide earthquake dynamic rupture scenarios HE, HM, and HW are all initialized using the same laterally homogeneous Cartesian prestress tensor (see Sec. 2). We consider them as "worst-case" scenarios, since they yield high moment magnitudes of M_W ∼9 (Table 2). The three selected hypocenters are located on the eastern (below eastern Crete, model HE) and the western (below Peloponnese, model HW) part, as well as in the middle (between Crete and Peloponnese, model HM) of the megathrust interface (see Fig. 2). Depending on hypocentral location, the main rupture propagation mode varies from unilateral to west (HE) or east (HW) to bilateral to east and west for model HM. Scenario HW produces the largest maximum fault slip (15.93 m, Tab. 2, Fig. 2c) localized at intermediate depth (∼20–30 km) on the fault segment below south of Crete, which is ∼3.5 m higher than for scenario HE.

Including off-fault plastic deformation in our fourth dynamic rupture model (model HEP) leads to overall similar rupture characteristics (fault slip, peak slip rate, and rupture velocity) as for the purely elastic reference model HE (Tab. 2, Fig. B1). Nevertheless, rupture propagation is here limited to the deeper fault portion as off-fault plastic deformation efficiently inhibits rupture propagation to the sediments (upper 15 kms). The accumulated plastic strain surrounding the HA megathrust generates a flower-shaped structure with depth (Wirp et al., 2024).

In the fifth scenario, model HEA, the rupture propagation is restricted by the assumed initial stress asperity. Thus, the rupture arrests after ∼60 s simulation time. Model

HEA produces the smallest moment magnitude of ∼8 among all five scenarios. The maximum fault slip is 10.92 m, which is ∼5 m smaller than in scenario HW and the maximum peak slip rate of 2.2 m/s is ∼5.7 m/s smaller than in scenario HE (Table 2, Figs. 2a-e and B1).

Model	**HE**	**HM**	**HW**	**HEP**	**HEA**
M_W	9.07	9.09	9.17	9.06	8.06
Avg. fault slip [m]	5.09	6.03	6.56	6.17	2.32
Max. fault slip [m]	12.55	14.30	15.93	12.71	10.92
Avg. peak slip rate [m/s]	1.40	1.51	1.77	1.40	0.68
Max. peak slip rate [m/s]	7.87	6.76	6.69	6.90	2.20
Avg. rupture velocity [m/s]	3373	3283	3341	3398	2413
Max. rupture velocity [m/s]	5379	5379	5375	5372	4562
Rupture time [s]	177	160	198	180	59
Computational cost [CPUh] for 300 s simulation time	190,400	185,920	141,680	158,480	187,040
Max. seafloor uplift [m] (after Tanioka filter)	9.46	8.02	9.34	10.22	1.91
Max. sea-surface height anomaly [m]	4.31	4.13	4.39	6.58	1.55

Table 2. Key results of our here considered five earthquake dynamic rupture scenarios, see also Wirp et al. (2024).

3.1.2 Static bathymetry perturbation

Figure 2f-j shows the bathymetry perturbation used as input in the tsunami models resulting from the accumulated seafloor deformation in the five dynamic rupture simulations. The margin-wide dynamic rupture scenarios with varying hypocentral locations HE, HM, and HW are similar in magnitude but show remarkable differences in the induced seafloor displacement and associated bathymetry perturbation (see Fig. 2f-h). While all three scenarios develop similar primary uplift and subsidence features collocated with high on-fault slip, we observe additional narrow bands of uplift near the trench that differ in their length and are associated with rupture propagation into the shallow slip-strengthening region of the subduction interface. The direction of rupture propagation controls the amount of shallow slip, resulting in the largest uplift band for a western hypocenter (scenario HW).

Enabling off-fault plastic yielding in our model (HEP) inhibits rupture propagation into the shallow slip-strengthening part of the fault interface but leads to a higher amount of vertical seafloor uplift (maximum 10.22 m) south of Crete. Applying a single prestress asperity to the initial loading (model HEA) limits rupture extent and fault slip amplitudes. In this case, a maximum uplift of 1.91 m is located southeast of Crete.

3.1.3 Nonlinear shallow-water tsunami simulations sourced by static seafloor displacement

The tsunami simulation domain (Figs. 3, 4) covers large parts of the Mediterranean, including the islands of Corsica and Sardinia in the west, the eastern Italian and Croatian coasts in the north, the African coasts of Tunisia, Libya, and Egypt in the south, and the whole eastern Mediterranean Sea, covering the Turkish coast, Syria, and Israel.

Fig. 3 shows snapshots of the tsunami evolution after 0.5 h, 1.5 h, and 2.5 h simulation time. The first column represents the early stage of tsunami generation after 0.5 h. We define the deviation of the sea surface from the ocean at rest as sea surface height

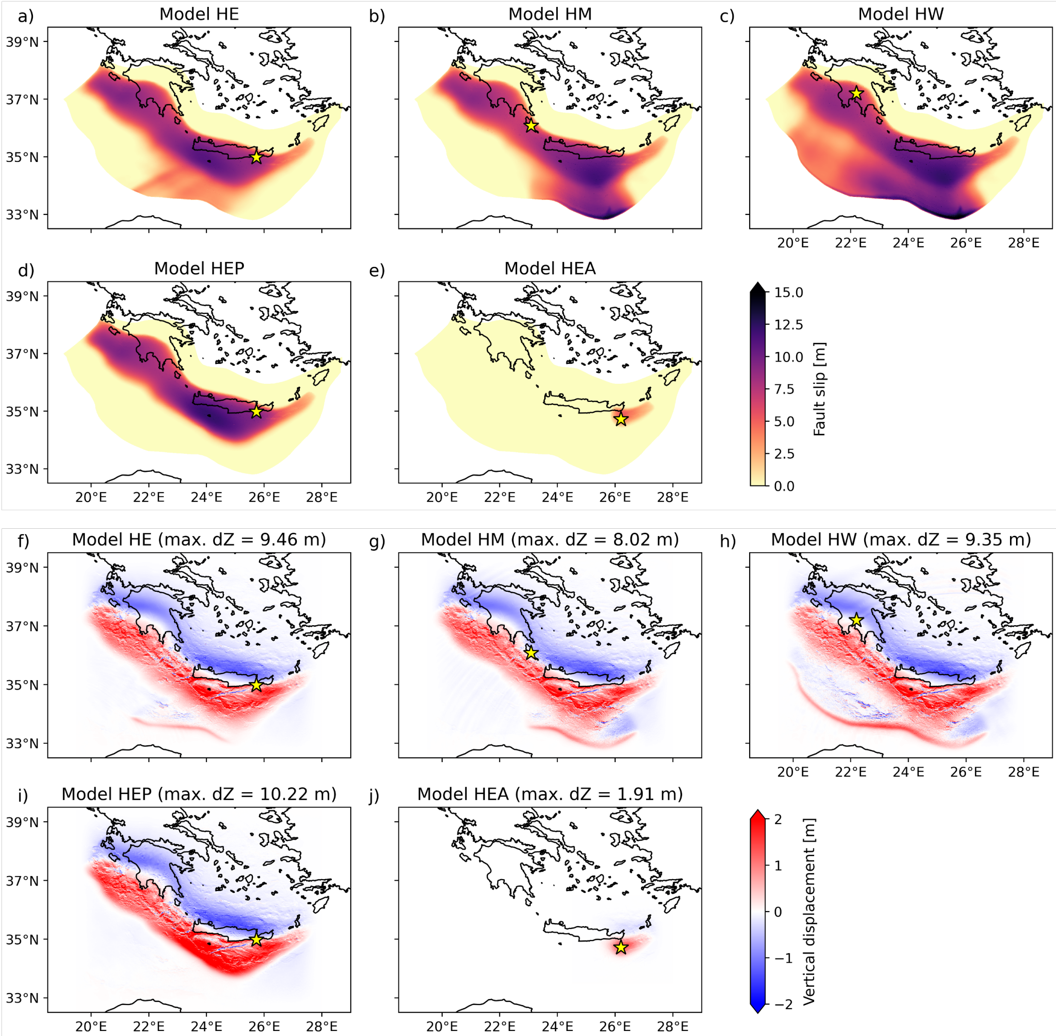

Figure 2. Accumulated fault slip at the end of five SeisSol dynamic rupture simulations for models a) HE, b) HM, c) HW, d) HEP, e) HEA. Depending on the hypocentral location, fault slip penetrates the shallow slip-strengthening fault portion, causing a pronounced band of near-trench uplift. Yellow stars mark the hypocenters. **Computed bathymetry perturbation** used as input in the tsunami models associated with the earthquake dynamic rupture simulations for margin-wide rupture scenarios based on laterally homogeneous initial stress conditions f) HE, g) HM, h) HW, i) HEP including off-fault plastic strain and j) the single initial stress asperity approach (HEA). It combines the vertical surface displacement with the contribution from the horizontal displacement from the Tanioka filter (Tanioka & Satake, 1996). Max. dZ refers to the maximum bathymetry perturbation of each scenario. Note the thin band of near-trench uplift in panels f), g), and h) produced by slip penetrating the shallow slip-strengthening fault region (see a), b), c)).

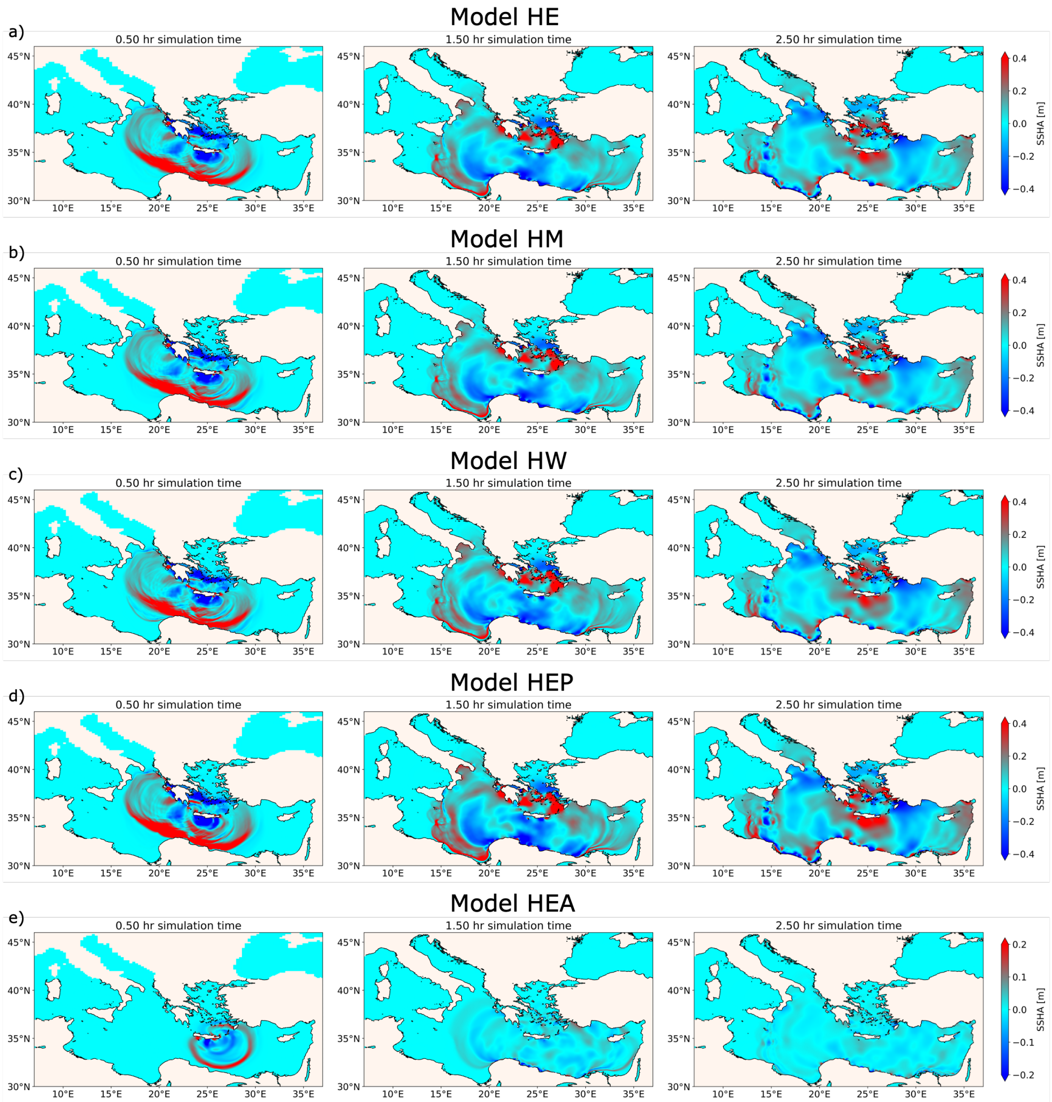

Figure 3. Sea surface height anomaly (ssha) of all five one-way linked earthquake-tsunami scenarios at 0.5 h (first column), 1.5 h (second column), and 2.5 h (third column) simulation time. The initial coarse grid in the North (see 0.5 h simulation time) is refined with increasing simulation time. Note the different color scale for panel **e)**.

anomaly (ssha [m]). In the early stage, the tsunami evolution does not differ much between the four margin-wide rupture scenarios HE, HM, HW, and HEP, despite the differences in max. amplitudes of ssha (Fig. 4). 0.5 h after all four earthquakes, a tsunami leading front of ∼1.25 m height reaches the North African coasts of Libya and Egypt. In all four margin-wide models, the tsunami has reached most parts of the Cyclades, south Aegean, Crete, the Dodecanese, and the Ionian Islands, as well as large parts of the western Greece coasts are affected by the tsunami. After 1 h, a smaller tsunami front propagates in the northwest direction through the Ionian Sea towards southern Italy and the east direction through the Levantine Sea. Smaller wave heights of ∼0.2-0.5 m approach Sicily and Cyprus, while the main tsunami front travels towards the east and west direction along the African coast. After 2-2.5 h simulation time, the tsunami reaches the eastern Mediterranean coasts and approaches the northern Aegean islands. We see complex wave interaction with the coasts, superposition, and waves being trapped between the Greek islands (Fig. 3, third column). For the western Mediterranean coasts, no tsunami waves of significant amplitudes are observed. The tsunami kinematics among models HE, HM, HW, and HEP are overall similar. The main difference when including off-fault plastic deformation in model HEP is that the maximum values of ssha are up to 2.27 m higher, while the wave propagation evolution is similar to the purely elastic model (HE). Later, differences in the tsunami wave propagation are barely visible (Figs. C1, C2, C3, C4). The tsunamis reach the western boundaries of the model area after ∼8 h simulation time.

In the non-margin wide scenario HEA, the ensuing tsunami differs greatly from the four margin-wide rupture scenarios (Figs. 3e, C5). The tsunami waves of max. ∼0.5 m reach the African coast later than in the other models, after ∼0.75 h simulation time, and approach Sicily island after ∼2 h with heights of ∼0.1 m. The tsunami waves reach the Cyclades after 0.5 h simulation time, but act like a shield for the north Aegean islands. Likewise, in scenarios HE, HM, HW, and HEP, we observe a complex wave interaction with the African coasts and superposition of waves (Fig. 3e, second and third column).

Figure 4 shows the maximum ssha over 8 h simulation time for all five dynamic rupture scenarios (Animations S1, S2, S3, S4, and S5). Grey lines mark the wave propagation expansion after 1 h, 2 h, 3 h, 4 h, 5 h, and 6 h, respectively. The maximum ssha highlights differences among the tsunami of the margin-wide rupture scenarios. They mainly differ in tsunami heights south of Crete, between the African coasts and Crete island. The contribution from the small band of near-trench seafloor uplift (see Sec. 3.1.2, Fig. 2) that varies with hypocentral location can be identified in the maximum ssha distribution, south of Crete. This feature is most pronounced for model HW and smallest for model HM among the margin-wide homogeneous initial pre-stress scenarios, and explains why larger tsunami amplitudes of ∼4.4 m are resulting from scenario HW, while in model HM, smaller wave amplitudes of ∼4.1 m are observed.

The differences in ssha associated with the small band of near-trench seafloor uplift are also visible in the tide gauges around Crete (Figs. C6, C7, C8). The gauge stations south and west of Crete report remarkable differences in ssha, while north-east of Crete the ssha is similar for different hypocentral locations (i.e., gauge 5). For example, gauge 12 reports a maximum deviation of the sea surface height of ∼2.2 m for the eastern hypocenter (model HE), while for the western hypocenter (model HW) this height is reduced to ∼2 m and ∼1.7 m for the middle hypocenter (model HM). For larger distances (Figs. C6, C7, C8 gauges 17-23), the differences in tsunami arrival and height between the models are marginal.

In model HEP, unconsolidated sediments in the upper 15 km of the seafloor enhance the seafloor displacement and result in the largest tsunami amplitudes, reaching maximum values of ∼6.6 m south-west Crete (Fig. 4 d). A tsunami front of more than 2.5 m height reaches the North African coast after ∼1 h simulation time (Fig. C9, gauge 22).

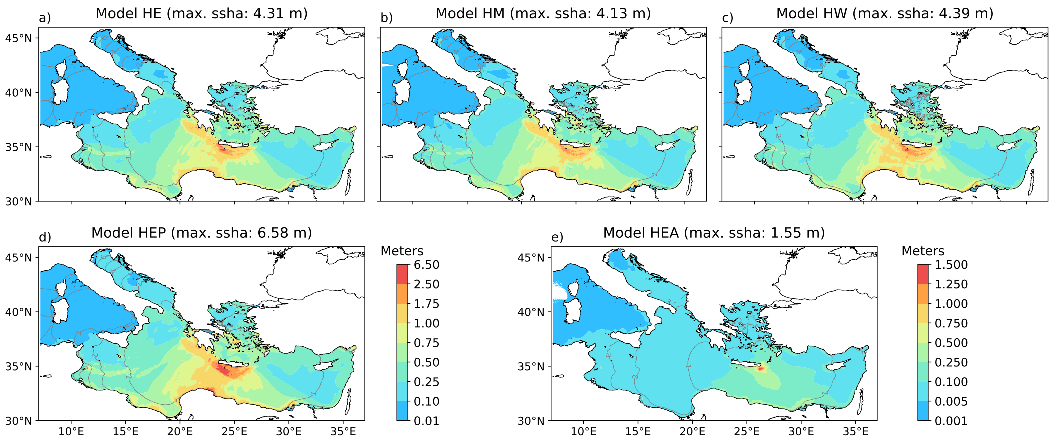

Figure 4. Maximum sea surface height anomaly (ssha [m]) in the Mediterranean during the simulation time of 8 h for five non-linear shallow water equation tsunami simulations induced by static bathymetry perturbations computed from the coseismic displacement of five dynamic rupture scenarios. The contour lines show the tsunami propagation expansion after 1 h, 2 h, 3 h, 4 h, 5 h, and 6 h, respectively. In **a)** model HE, **b)** model HM, and **c)** model HW, the epicenter location in the dynamic rupture models is varied (Fig. 2), **d)** model HEP allows for off-fault plastic deformation in the upper 15 km, and **e)** model HEA uses a single initial stress asperity. Note the different color scale for panel **e)**. See Animations S1, S2, S3, S4, and S5 for illustrations of the time-dependent evolution of ssha.

For model HEA, tsunami amplitudes are the smallest. This $M_W 8$ scenario produces maximum wave amplitudes of 1.55 m southeast Crete island (Fig. C10, gauge 9). The tsunami approaches the North African Coast with a height of $\sim$0.5 m. The Mediterranean coasts west of Crete island, east of Cyprus island, and north of the Cyclades are barely affected by the tsunami.

3.2 3D fully-coupled scenario

We extend model HE into a fully-coupled earthquake-tsunami scenario. Due to the high computational cost, simulation time is chosen shorter than the shallow-water models to 300 s, which allows capturing the dynamic tsunami generation phase and the beginning of the tsunami propagation, but does not allow comparing it with the full tsunami evolution simulated by the one-way linked approach. Figure 5 shows the tsunami evolution of the fully-coupled model after 150 s simulation time. During rupture propagation, seismic waves are generated in the solid, elastodynamic part of the model domain. These waves interact with the acoustic waves being generated in the water layer and with the time-dependent seafloor displacement close to the source. Acoustic and seismic waves superimpose at the early tsunami generation stage in the near-fault region (panels a) and b) of Figs. 5, D1, D2, D3, and Animation S6) and at a later stage also close to the edges of the simulation domain (Fig. D4a). We select three profiles perpendicular to the average strike of the megathrust and plot the ssha across these profiles (Figs. 5, D1, D2, D3, D4, D5 c) to better understand the complex superposition of the different wave types. We observe high-amplitude seismo-acoustic waves in the early tsunami generation stage. The acoustic waves are much faster than the actual tsunami and reach the southern simulation bands after 100 s simulation time. Panels (b) show the sea surface vertical velocity (ssvv) in [m], dominated by the acoustic waves rather than by the tsunami waves (Kutschera, Gabriel, et al., 2024). At 300 s simulation time, 100 s before the timestep that is used to source the tsunami simulations in the one-way linked approach (Sec. 3.1.3), the tsunami has already begun propagating in the fully-coupled model (Fig. D5 and Animation S7). The narrow near-trench uplift band identified in Fig. 2f-h is much less obvious in the fully-coupled model, and may have been filtered out by the ocean layer response due to its short wavelengths.

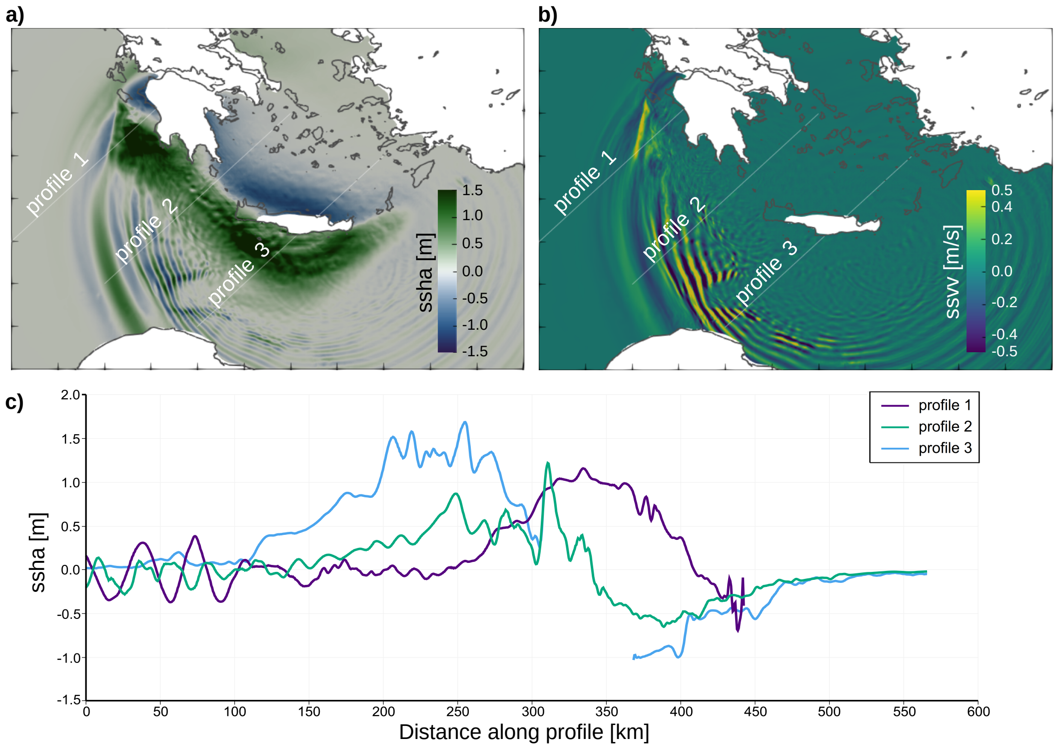

Figure 5. Large-scale 3D fully-coupled earthquake-tsunami scenario (HE). a) Sea surface height anomaly (ssha) after t =150 s simulation time. b) Sea surface vertical velocity (ssvv) after t =150 s simulation time. c) Sea surface height anomaly (ssha) along three selected cross-sections (profiles 1–3). See Animations S6 and S7 for illustrations of the time-dependent evolution of ssha and ssvv.

3.2.1 Tide gauges and Spectrograms

Analysis of synthetic time series at virtual near-coast tide gauges shows directivity effects and locally large amplitudes of acoustic waves generated during tsunami initiation.

Figure D6 shows the vertical velocity of the water column recorded at 11 synthetic tide gauge stations (red triangles in Figure 6 b). We observe acoustic waves reaching the stations located on the Crete coast during the early tsunami generation stage, ∼30–60 s after rupture onset. As the on-fault rupture propagates from east to west, they are first recorded at stations 13 and 14 located on eastern Crete, and later at stations 15 and 16 that are situated on western Crete. The maximum ssvv due to the acoustic waves recorded at gauges 13 and 14 is ∼0.03–0.05 m/s. In the records of stations 15 and 16, the first arrival of the acoustic wave is more pronounced, reaching a maximum of 0.4 m/s at gauge 16. Stations 17 and 18 record much smaller acoustic wave velocities of 0.025–0.01 m/s arriving after ∼100 s simulation time. The rupture propagation direction across the Hellenic Arc is from east to west, causing a time-dependent seafloor displacement and tsunami generation also evolving from east to west (Figs. D1a, D2a). Thus, higher signals of ∼0.35–0.5 m/s are also recorded at gauges 19 and 22 that are located north- and southeast of Crete. For some stations, we observe the acoustic waves as very narrow peaks (gauges 14, 15, 16, 19), whereas at others they are recorded as broader signals (stations 13, 17, 18, 20, 21, 22, 23).

To analyze the time-dependent frequency content of simulated sea surface signals, we compute spectrograms of the tsunami vertical velocity for all near- and far-field gauge stations (Fig. 6). The signature of direct acoustic waves can be identified in the high-frequency leading waves. This signal is followed, for example, at receivers 13, 17, and 18, by dispersive waves, which we identify as oceanic Rayleigh waves (Oliver & Major, 1960; Kozdon & Dunham, 2014; Wilson & Ma, 2021), surface waves that propagate at the interface between ocean water and the underlying solid crust.

4 Discussion

4.1 Comparison with historic tsunamis

We compare our modeled tsunami scenarios to the historic AD 365 and 1303 Crete tsunamis. The margin-wide rupture models and resulting tsunami may plausibly reproduce historic events, as the modeled coseismic uplift matches observations and the simulated tsunami impacts the entire eastern Mediterranean, with a leading wave reaching the African coast and Nile delta. The AD 365 earthquake and tsunami, key events governing Mediterranean tsunami hazard, have been extensively studied (e.g., Shaw et al., 2008; Yolsal-Çevikbilen & Taymaz, 2012; England et al., 2015; S. Tinti et al., 2005; Bahrouni et al., 2024). While the event is generally agreed to have ruptured a dip-slip fault rather than the megathrust, dynamic rupture models suggest its resulting seafloor displacement could have been caused by a margin-wide megathrust event (Wirp et al., 2024), specifically by an earthquake resembling model HEP that includes large off-fault plastic deformation. Tsunami deposits of the AD 365 earthquake were found in western Crete, close to the ancient harbor Phalasarna (Pirazzoli et al., 1992). Paleoshorelines at the eastern Crete island edge suggest a coseismic uplift of up to ∼10 m which reduces towards the north-east (Flemming, 1978; Pirazzoli et al., 1982, 1996; S. Stiros & Drakos, 2006; Shaw et al., 2008), with tsunami deposits potentially associated to this event reported also in Tunisia (Bahrouni et al., 2024), and in Eastern Sicily (De Martini et al., 2010). The corresponding tsunami destroyed many towns on Crete island and hit most of the eastern Mediterranean coasts, including northern Africa up to the Nile delta (S. C. Stiros, 2020). S. Tinti et al. (2005), Shaw et al. (2008), and Yolsal-Çevikbilen and Taymaz (2012) model the tsunami propagating from the source to the opposite side of the Mediterranean Sea, reaching the African coasts, sweeping west- and eastward towards Tripolis and the Nile Delta.

The tsunamis sourced by our margin-wide rupture scenarios show highest amplitudes around Crete, Rhodes, the southern Aegean, eastern Libya, and Egypt, while the western Mediterranean is barely affected by the tsunami, which is in agreement with S. Tinti et al. (2005). The margin-wide rupture models predict edge waves along the African coast amplified by shoaling effects (Shaw et al., 2008), which are waves traveling along the shoreline and confined by the sloping seabed. Sardinia is being mainly shielded by Sicily and the land mass of Tunisia, and on a dominant curved band of locally high maximum ssha south of Malta. The initial coseismic uplift of ∼8-10 m induced by the margin-wide models southeast Crete fits the seafoor displacement of 10 m that was inferred from topography changes, seamarks, and fallen blocks (Spratt, 1865; Flemming, 1978; Pirazzoli et al., 1982; S. Stiros & Drakos, 2006) associated with the AD 365 event. The similarity between models HE, HM, and HW of different hypocentral locations highlights the difficulty in identifying a source location for historical events.

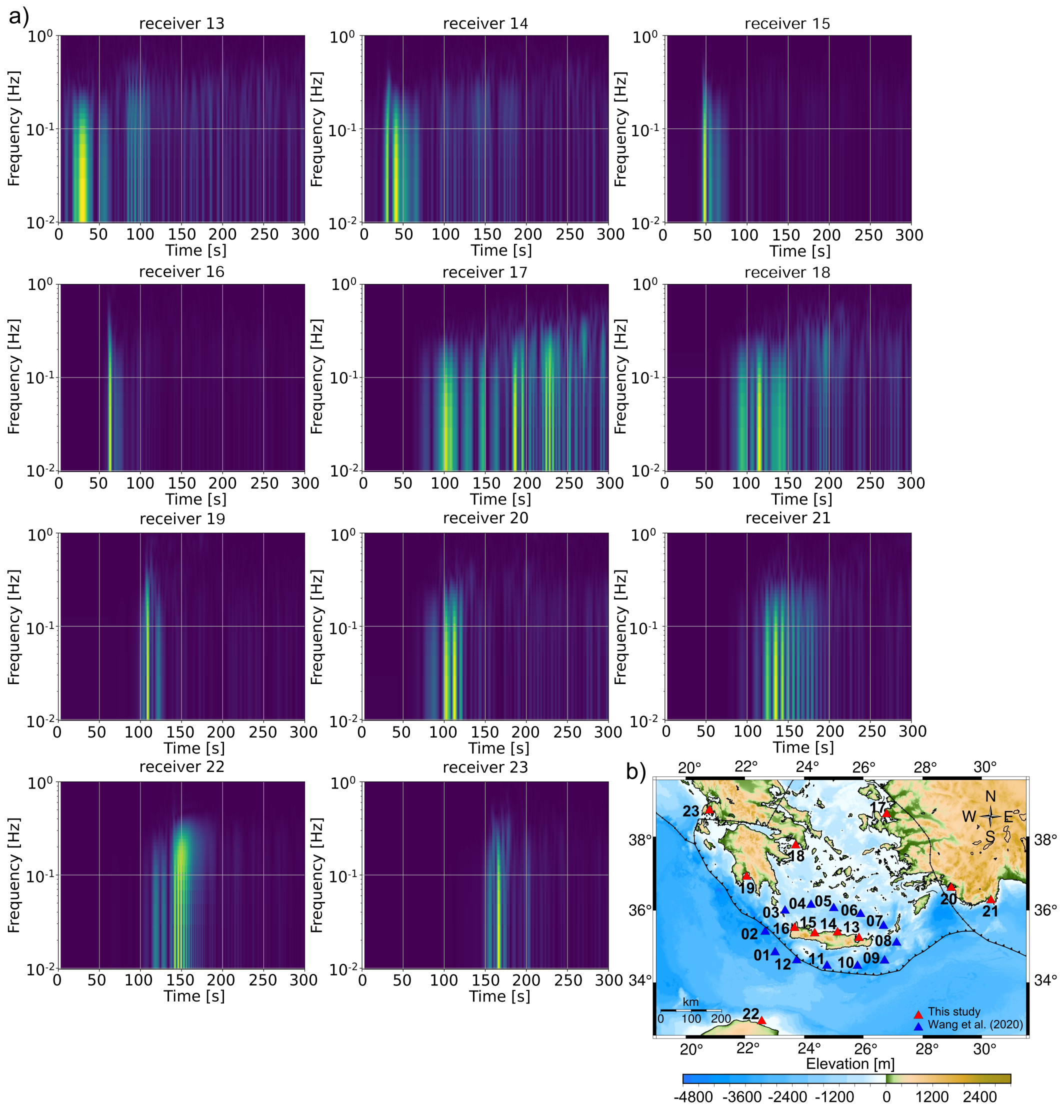

Figure 6. a) Spectrograms of acoustic signals recorded at the 11 tide gauge stations (b) in the fully-coupled earthquake-tsunami simulation. The signature of direct acoustic waves can be identified in the high-frequency leading waves. This signal is followed at stations 13, 17, and 18 by dispersive waves, which we identify as oceanic Rayleigh waves (Oliver & Major, 1960). b) Map showing the tide gauge locations used in this study. Blue triangles mark the tide gauge stations from Wang et al. (2020), while red triangles are the stations added in this study.

The tsunami caused by the 1303 Crete earthquake has also been the focus of several earlier studies (e.g., Yolsal et al., 2007; Yolsal-Çevikbilen & Taymaz, 2012; England et al., 2015; S. Tinti et al., 2005). It affected the Greek Islands and Peloponnese, propagating north and directing to southwest Turkey, reaching Cyprus towards the east and the African coast to the south (Yolsal et al., 2007). For this event, Yolsal et al. (2007) model a maximum wave height of 7 m east of Crete. Such a high tsunami is among our models only feasible for an M_W ~9 event breaking the entire Hellenic Arc megathrust (model HEP). The tsunami evolution modeled by Yolsal et al. (2007) is similar to our margin-wide rupture scenarios (HE, HEP), both in terms of kinematics and wave heights. Wirp et al. (2021) identify the elastic model with eastern hypocenter (HEA) to resemble the location and magnitude of the 1303 tsunamigenic event. However, while our tsunami simulation (Figs. 3e, 4e and Animation S5) sourced by model HEA produces a realistic distribution of ssha, it does not reproduce the high tsunami amplitudes inferred for the event, likely due to its too deep slip. This means that a $M_W \leq 8$ megathrust event is unlikely to resemble historical tsunami records.

4.2 Implications for regional and transnational tsunami hazard assessment

The active margin of the Hellenic Arc with average repeat times of 66 years for M_W7.0 earthquakes poses a high seismo- and tsunamigenic potential (G. A. Papadopoulos & Kijko, 1991; G. Papadopoulos et al., 2012). This highlights the need for seismic and tsunami hazard assessment in the region and in distant areas potentially impacted by tsunami caused by earthquakes on the Hellenic Arc megathrust (e.g., Okal et al., 2009; Yolsal et al., 2007; Sørensen et al., 2012; Yolsal-Çevikbilen & Taymaz, 2012; Coban & Sayil, 2020; Basili et al., 2021; Triantafyllou et al., 2024). The NEAM Tsunami Hazard Model 2018 (NEAMTHM18) (Basili et al., 2021), for example, is a probabilistic hazard model covering the Mediterranean, and making use of stochastic models to explore a large tsunami source variability (Scala et al., 2024). They use both, seismicity-based and tectonic models (e.g., Davies et al., 2018), together with depth-dependent subduction and rupture properties, including the potential for shallow slip amplification (e.g., Murphy et al., 2016).

However, the absence of digital records of large tsunamigenic earthquakes on the Hellenic Arc megathrust together with long return periods and uncertainties about fault geometries and properties hinder the understanding and correct assessment of earthquake and tsunami hazard studies in this area (e.g., Shaw et al., 2008; Ganas & Parsons, 2009; Vernant et al., 2014; England et al., 2015). Dynamic rupture simulations of megathrust earthquakes may contribute to reducing the epistemic uncertainty associated with tsunami hazard analysis. The models use physically consistent initial conditions that could help reduce the random variability of stochastic slip models. Dynamic rupture model also provides time-dependent initial seafloor displacements for tsunami simulations, which may remove some biases due to simplifying assumptions of instantaneous and static tsunami initial conditions. Such models can help in refining stochastic and probabilistic tsunami hazard assessments (e.g., Murphy et al., 2016; Savran & Olsen, 2020), with additional physically viable earthquake scenarios (Ripperger et al., 2008; Schmedes et al., 2010), and adding the resulting tsunami adds additional observables to validate dynamic rupture (e.g., Davies, 2019; Ulrich et al., 2022).

The dynamic rupture examples presented here focus on (worst-case) M_W8+ megathrust earthquakes. Their corresponding tsunami exemplify that the main megathrust should be taken into account when calculating the hazard for surrounding areas and regions that lie further away, for example, the Italian and northern African coasts. Our results show overall higher tsunami amplitudes to the South, exceeding 1 m along the northern coast of Egypt and Libya, which is in agreement with current operational tsunami hazard models using thousands of simpler models (Basili et al., 2021). However, balancing the required source variability, including smaller earthquakes, for probabilistic tsunami simulations with the feasible number of simulations remains a challenge, particularly for dynamic rupture simulations, which are inherently computationally expensive.

4.2.1 Shallow water and instantaneous sourcing tsunami modeling assumptions

In Table 3, we follow Abrahams et al. (2023) and summarize several non-dimensional parameters that allow us to assess the validity of simplifying modeling assumptions for our tsunami model setup. These parameters control the solution behavior for a Gaussian source. Assuming a source width of σ_r =100 km, the shallow water approximation

$$H/\sigma_r \ll 1 \tag{6}$$

is valid everywhere within our model domain given that the maximum water depth of the Aegean is H =3,544 m close to Crete. We further consider a source duration σ_t of 180 s for model HE. For

$$H/(c_0 \cdot \sigma_t) \ll 1 \tag{7}$$

the contribution of acoustic waves to the tsunami should theoretically be negligible. Assuming an instantaneous source is appropriate if

$$\sqrt{gH} \cdot \sigma_t/\sigma_r \ll 1\,, \tag{8}$$

with c_0 =1500 m/s being the acoustic wave speed and g =9.81 m/s^2 the gravitational acceleration. In the case of all our scenarios, this condition is not fulfilled. Applying instantaneous sourcing will omit a potentially non-negligible amplitude of acoustic waves during tsunami generation, as illustrated in our fully coupled scenario.

Source width σ_r (m)	Source duration σ_t (s)	Shallow water limit $H/\sigma_r \ll 1$	Negligible acoustic wave excitation $H/(c_0 \cdot \sigma_t) \ll 1$	Instantaneous source $\sqrt{gH} \cdot \sigma_t/\sigma_r \ll 1$
100,000	180	Valid	Valid	0.33

Table 3. Non-dimensional parameters for our model setup, as introduced by Abrahams et al. (2023). c_0 =1500 m/s is the acoustic wave speed g =9.81 m/s^2 the gravitational acceleration and H is the maximum water depth of the Aegean east of Crete (∼3,544 m).

4.3 Source spectrum analysis of oceanic acoustic and tsunami waves

Kozdon and Dunham (2014) identify normally and anomalously dispersed Rayleigh waves in their 2D fully-coupled dynamic rupture-tsunami simulations of the 2011 Tohoku-Oki earthquake in the Japan Trench. They showcase the complex oceanic wavefield, which might be recorded by ocean bottom seismometers, including large-amplitude waves that propagate slower than the ocean sound speed. Similar waveform characteristics have been observed in 2D fully-coupled simulations of Cascadia earthquake and tsunami scenarios by Wilson and Ma (2021). They find that the excitation of oceanic Rayleigh waves changes with the amount of shallow rupture. Abrahams et al. (2023) analyze the acoustic signals generated in simplified 3D fully-coupled earthquake tsunami simulations. They identify initially arriving normally dispersed long-period oceanic waves that leak oceanic P-wave modes, the "PL" waves (Oliver & Major, 1960; Kozdon & Dunham, 2014; Wilson & Ma, 2021), which are followed by wave packets of Rayleigh waves. They show that the wave spectra vary with direction from the source due to directivity effects.

In our 3D fully-coupled simulation, we observe high-frequency leading acoustic waves, followed by packets of dispersed oceanic Rayleigh waves, similarly to previous work. We observe the maximum ssvv (sea surface vertical velocity) of acoustic waves depending on the location of the gauge stations relative to the rupture direction from the source (Figs. 6b, D6). Stations located in the rupture propagation direction (e.g., stations 15, 16, 19, 22) record more pronounced and up to 90% higher acoustic amplitudes than stations located on the opposite side of the megathrust (e.g., stations 20, 21).

We extract the vertical velocity of the sea surface along the three profiles from Fig. 5b, with their respective spatio-temporal evolution shown in Fig. 7. We observe a dominant, fast-traveling wavefront at 3000 ms^{-1} (black dashed line) wave speed in profile 3. Signals with the same wave speed are visible in profiles 1 and 2 as well. Due to the long source duration of 180 s for the margin-wide rupture model HE, the tsunami source is not instantaneous (Eq. 8) and acoustic signals could be emitted during the tsunami generation phase. Acoustic signals, propagating at c_0 =1500 ms^{-1} (red dashed line) can be identified in profile 1 and 2. All three profiles show multiple signals (light blue dashed line) propagating at speed of around 80 ms^{-1}, corresponding with the expected speed of a tsunami propagating in a 640 m shallow water layer. The amplitudes of the sea surface vertical velocity of the fast-propagating primary wavefront are $\sim$2.5 m/s larger than the actual tsunami amplitudes. For profiles 1 and 2, the acoustic wave amplitudes are $\sim$0.5 m/s and as large as those corresponding to the tsunami. Since the average depth of the water H is much smaller than $c_0 \cdot \sigma_t$ (Table 3), we would expect from simplifying analysis that the amplitudes of the acoustic waves should be negligibly small (Abrahams et al., 2023). However, in our realistic 3D model setup, this is only the case for profile 3, where the acoustic wave amplitudes remain smaller than 0.5 m/s. In distinction, profiles 1 and 2 include acoustic waves with ssvv amplitudes comparable to the respective gravity tsunami waves amplitudes, up to $\sim$0.5 m/s in profiles 1 and 2. These unexpectedly high acoustic wave amplitudes may be due to the complex topo-bathymetry in the Mediterranean, since the conversion between seismic and ocean acoustic waves is assumed to occur mainly at slopes of the seafloor (Noguchi et al., 2013). None of our scenarios includes surface breaching ruptures, another common cause of high acoustic amplitudes during the tsunami generation phase (Abrahams et al., 2023), since the Hellenic Arc megathrust does not intersect with the seafloor.

The observed complex superimposition of sizable acoustic waves and tsunami waves in the near-field even in shallow water can challenge the understanding of the tsunami generation phase. However, in the far-field, high-amplitude acoustic waves may be useful as a “rapid indicator” of tsunamigenic earthquake rupture. At near-fault gauge stations, the amplitude of simulated acoustic waves is large enough to be extracted from tide gauge signals, and may help tsunami early warning before the arrival of the main tsunami wave. While beyond the scope of this work, a better understanding of how acoustic signals are linked to tsunamigenic seafloor motion can improve tsunami early warning, e.g. using ocean bottom pressure sensors or seafloor DAS (e.g., Yamamoto, 1982; Mei & Kadri, 2017; Gomez & Kadri, 2021; Becerril et al., 2025; Henneking et al., 2025).

4.4 Limitations

For the one-way linking approach, we do not account for time-dependent seafloor motions but translate the static seafloor uplift into a displacement of the water column, resulting in a sea surface elevation. As a result, time-dependent dissimilarities in the tsunami generation process are not resolved between margin-wide models of different hypocentral locations (models HE, HM, HW), and are not discussed in this paper. In future work, the time-dependent variations of the 3-dimensional coseismic seafloor displacement could be translated into 2-dimensional vertical bathymetry perturbations for tsunami modeling (e.g., Wendt et al., 2009; Lotto et al., 2017; Ulrich, Vater, et al., 2019; Madden et

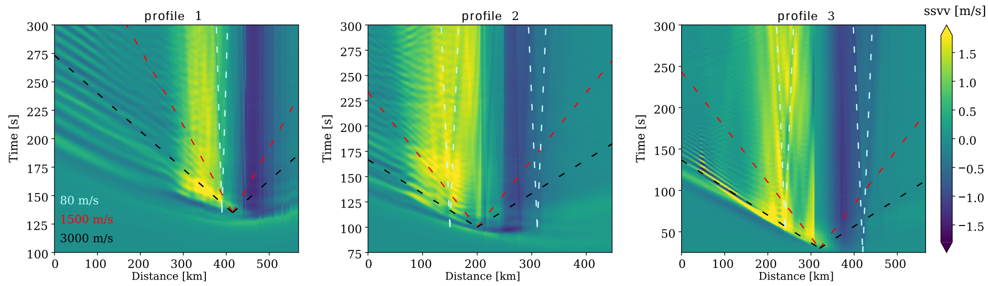

Figure 7. Space-time evolution of the sea surface vertical velocity (ssvv) for profiles 1, 2, and 3 of Fig. 5 for the full duration of the fully-coupled simulations. Dashed lines indicate velocities of 3000 m/s (seismic), 1500 m/s (acoustic waves), and 80 m/s (tsunami).

al., 2020; Wirp et al., 2021; Amlani et al., 2022; Kutschera, Gabriel, et al., 2024), utilizing temporal (Saito et al., 2019) or space-time Fourier filters (Madden et al., 2020).

Madden et al. (2020) show that the usage of a time-independent tsunami input can result in a later tsunami arrival at the coast, compared to a time-dependent source, together with a faster coastal inundation. However, Williamson et al. (2019) find that near-field one-way linked tsunami amplitude estimates are not significantly influenced by the assumption of instantaneous seafloor displacement. At the same time, recent work by Melgar (2025) has shown that tsunami amplitudes can increase by over 30% in the far-field when rupture duration and directivity are taken into account for large events ($M_W > 9.0$). However, the events studied by Melgar (2025) had primarily homogeneous slip, while the scenarios in this study are highly heterogeneous.

The one-way linked tsunami simulations are performed using the software GeoClaw (Berger et al., 2011; Gonzalez et al., 2011), a non-linear shallow-water tsunami solver. GeoClaw is currently in use for tsunami hazard assessment by several research groups (e.g., MacInnes et al., 2013; Borrero et al., 2015). Non-linear shallow water equations are the standard modeling method for tsunami propagation and run-up and the basis of other well-established tsunami codes, for example HySEA (Macías et al., 2017) and MOST (V. V. Titov & Gonzalez, 1997; V. Titov et al., 2016). These equations are less accurate for short wavelengths as the dispersive terms become more significant. Especially in near-shore regions, the tsunami flow evolves three-dimensionally, and the depth-averaged equations might become inaccurate. Boussinesq solvers, such as Funwave-TVD (F. Shi et al., 2012) and BoussClaw (Kim et al., 2017), can be used to incorporate wave dispersion. Even more accurate but computationally expensive would be the usage of fully-coupled earthquake-tsunami simulations for more than the one scenario presented here, which are able to capture the full tsunami generation phase and to model normal and anomalous dispersion (Sec. 4.3). Our fully-coupled simulation takes the time-dependent rupture propagation into consideration, but does not account for inundation and relies on a modified, simplified bathymetry. Since these models are computationally expensive due to the large simulation domain (Sec. 2.4) and the high resolution required to adequately resolve the tsunami, seismic, and acoustic waves. Thus, our fully-coupled simulation ran for a relatively short time (300 seconds), focusing on the generation phase of the tsunami.

Future computational optimization and improvement of computational resources (e.g., Panzera et al., 2016; Li et al., 2023; Folch et al., 2023) might allow running more of these fully-coupled models and running them for a longer simulation time. For now, we would advise using fully-coupled models only for selected extreme-scale scenarios, comparing with and translating the learned into less costly models for tsunami hazard assessment, which could be done with a two-step approach (Saito et al., 2019; Abbate et al., 2024; Abrahams et al., 2023).

5 Conclusions

We present five $M_W 8+$ megathrust earthquake-tsunami scenarios along the Hellenic Arc, including four margin-wide ruptures and one non-margin-wide event, all sourced from 3D dynamic rupture simulations. By sourcing tsunamis from physically consistent rupture scenarios, these models offer a way to reduce nonphysical variability in stochastic models and better constrain source parameters for probabilistic tsunami hazard assessment. While the four margin-wide scenarios share similar moment magnitudes, their induced seafloor displacements vary greatly: three margin-wide scenarios with different hypocentral locations but without off-fault plastic yielding cause slip to the trench, leading to small bands of near-trench uplift that vary in size, causing maximal displacements of 8.02 m–9.46 m. One scenario with plastic deformation inhibits rupture propagation into the shallow slip-strengthening region of the subduction interface, generating larger seafloor displacement away from the trench exceeding 10 m. These distinct uplift patterns caused by the varying rupture dynamics influence near-field tsunami amplitudes but have limited impact on far-field propagation, assuming instantaneous sources in nonlinear shallow water tsunami simulations. Maximum sea surface height anomalies (ssha) reach up to 4.4 m in the margin-wide scenarios, with energy focused along the Libyan and Egyptian coasts due to edge wave trapping, while the northern Aegean and western Mediterranean remain largely unaffected. Incorporating off-fault plastic deformation substantially enhances tsunami generation, increasing maximum ssha by more than 2 m and producing the largest modeled wave amplitudes, up to 6.6 m southwest of Crete. This enhanced tsunami response suggests that unconsolidated sediments and inelastic deformation may have played a critical role in amplifying historical events such as the AD 365 Crete tsunami. In contrast, the non–margin-wide $M_W 8$ scenario produces a maximum ssha of only 1.55 m, indicating that such megathrust events alone may be unlikely to account for the extreme wave heights inferred from historical records.

We demonstrate a large-scale 3D fully-coupled earthquake-tsunami simulation that integrates dynamic rupture, seismic and acoustic wave propagation, and tsunami generation. Using large-scale supercomputing and overcoming meshing challenges, we are able to perform this fully coupled model across a large, realistic domain, covering the Greek islands, the western Greek coast and Peloponnese, the Turkish coast to Kumluca, and parts of the Libyan coast. The fully-coupled approach is computationally expensive ($\sim$1 million CPU hours for 5 minutes simulation time), limiting its use here to one selected scenario. However, it can inform and calibrate cheaper models. Tsunami signals recorded at near and far tide gauge stations exhibit complexities not represented in one-way linked tsunami models. Therefore, we confirm that large earthquakes with long-duration ruptures ($\sim$180 s) and depth-dependent dispersion affect tsunami initiation. The fully-coupled simulation captures early-phase complexities of tsunami genesis, including acoustic and seismic waves and their transitions into tsunami motions. This superposition complicates signal attribution and may pose challenges to early warning systems and waveform inversion. However, the fully-coupled model also captures large-amplitude acoustic waves and oceanic Rayleigh waves, which arrive earlier than the main tsunami and are recorded as leading signals in near-field gauges, suggesting potential utility for early warning if detected by Mediterranean ocean-bottom pressure sensors or hydrophones.

Appendix A Meshing challenges

We build a complex structural model, incorporating the Hellenic Arc megathrust, topography, bathymetry, and the sea surface, and we generate high-quality unstructured tetrahedral meshes from this complex structural model using SimModeler (Simmetrix Inc., 2017). Incorporating a sea surface layer intersecting with a finely sampled bathymetry-topography surface is challenging, but is required for fully-coupled models.

This water layer is necessary to include the acoustic medium (Ocean) on top of the elastic (Earth) dynamic rupture model. To facilitate the calculation of the intersection, we resolve both the sea and bathymetry-topography surfaces with roughly similar mesh sizes in the structural model before calculating the intersection in SimModeler. This strategy has proven effective, although the large number of elements on the surface to be intersected can still pose challenges.

To further improve the intersection process, we smooth the topography using a Gaussian kernel with $\sigma = 1$ and adjust bathymetry nodes with $|z| < 200$ m to ± 200 m, reducing the risk of near-coplanar intersections. However, the software can still require manual adjustments when intersecting seafloor and sea surfaces in certain configurations.

An extensive and complex region such as the Hellenic Arc includes many of those challenging configurations: small-scale features in the topography, such as small islands or regions with shallow seafloor that lie close to sea level, did indeed challenge the intersection process and forced us to remove many of them. This simplification results in a more streamlined coastline representation in the 3D fully-coupled model. Moreover, we had to restrict the water layer to a smaller area to reduce the high computational costs associated with the oceanic acoustic and tsunami wave simulation (see Fig. A1). For the pure dynamic rupture models, we remove the water layer from the unstructured tetrahedral mesh, such that the bathymetry and resolution of the fully-coupled model are the same as for the one-way linked workflow.

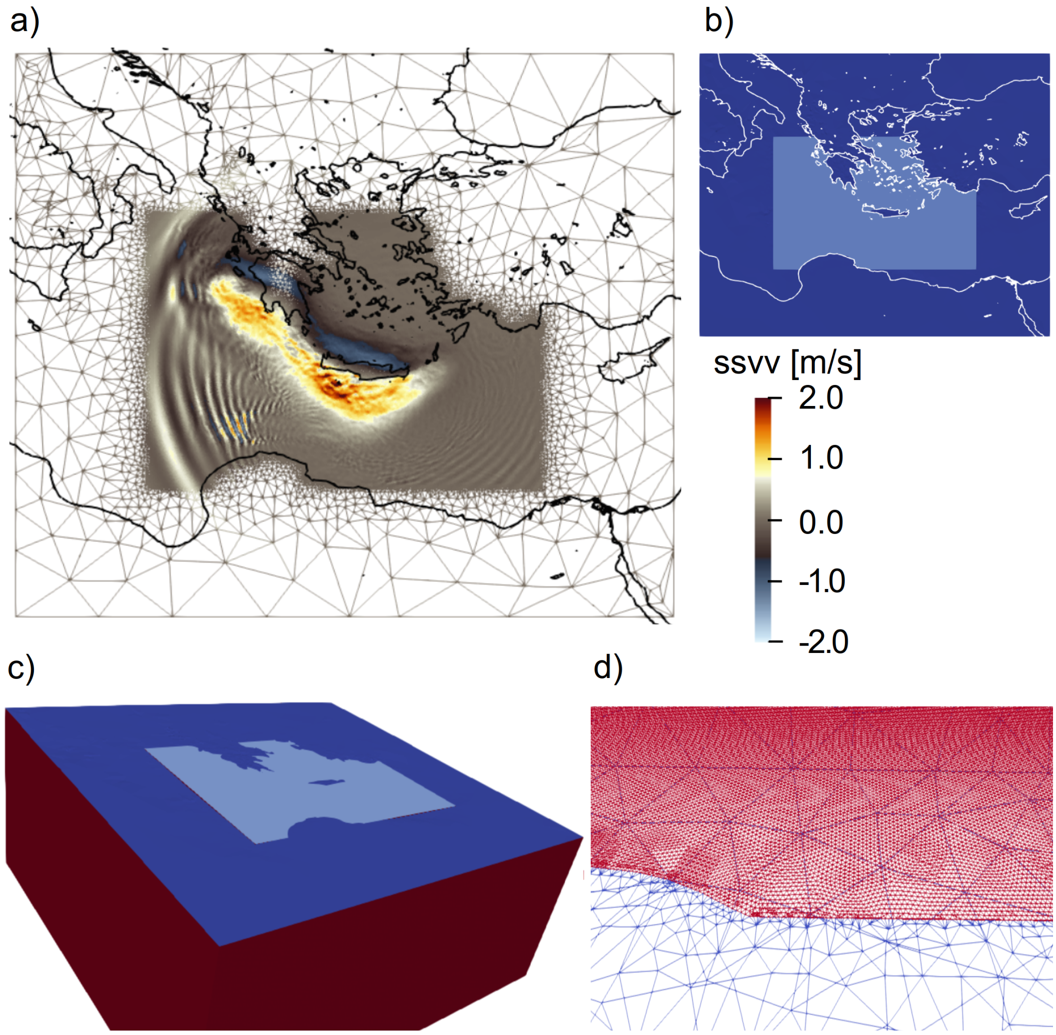

Figure A1. a) Computational mesh of the fully-coupled earthquake-tsunami model, including the water layer. The sea surface vertical velocity after 200 s simulation time ranges from -2 to 2 m/s to highlight complexities in the early stage of tsunami generation. Note that the modeling domain of the fully-coupled tsunami model is smaller than the one used with GeoClaw (Figs. 3 and 4). b) Map view and c) perspective view of the modeling domain of the fully-coupled model. The water layer is colored light blue, the free surface and absorbing boundary conditions are colored dark blue and red, respectively. d) Zoom into the connection of the water layer (red) and surroundings (blue). Note the finer mesh resolution of the water layer and the mesh size coarsening away from the water layer.

821 ## Appendix B Dynamic rupture modeling results

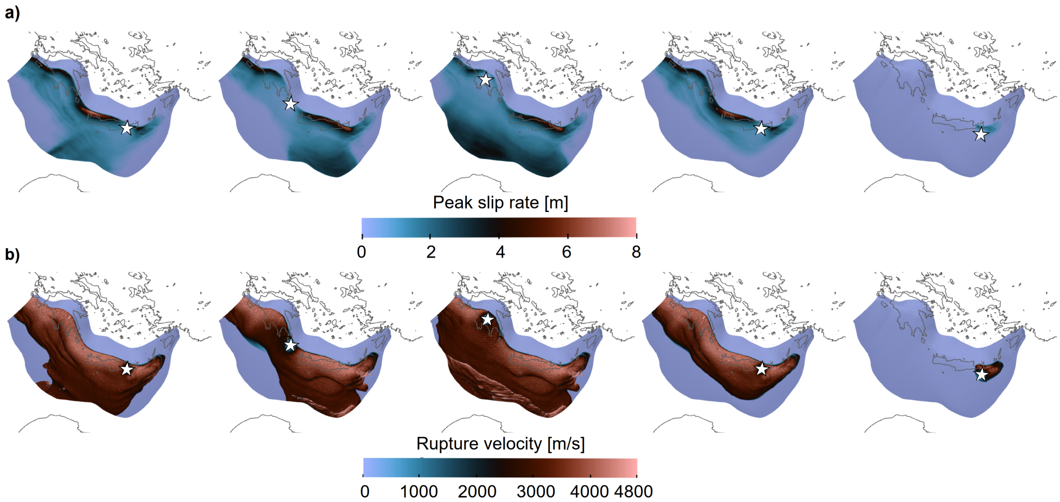

Figure B1. SeisSol dynamic rupture results: a) Peak slip rate and b) rupture velocity for models HE, HM, HW, HEP, and HEA, respectively. Depending on the hypocentral location, fault slip penetrates the shallow slip-strengthening fault portion, causing a pronounced band of near-trench uplift. White stars mark the hypocenter.

822 # Appendix C One-way linked tsunami results

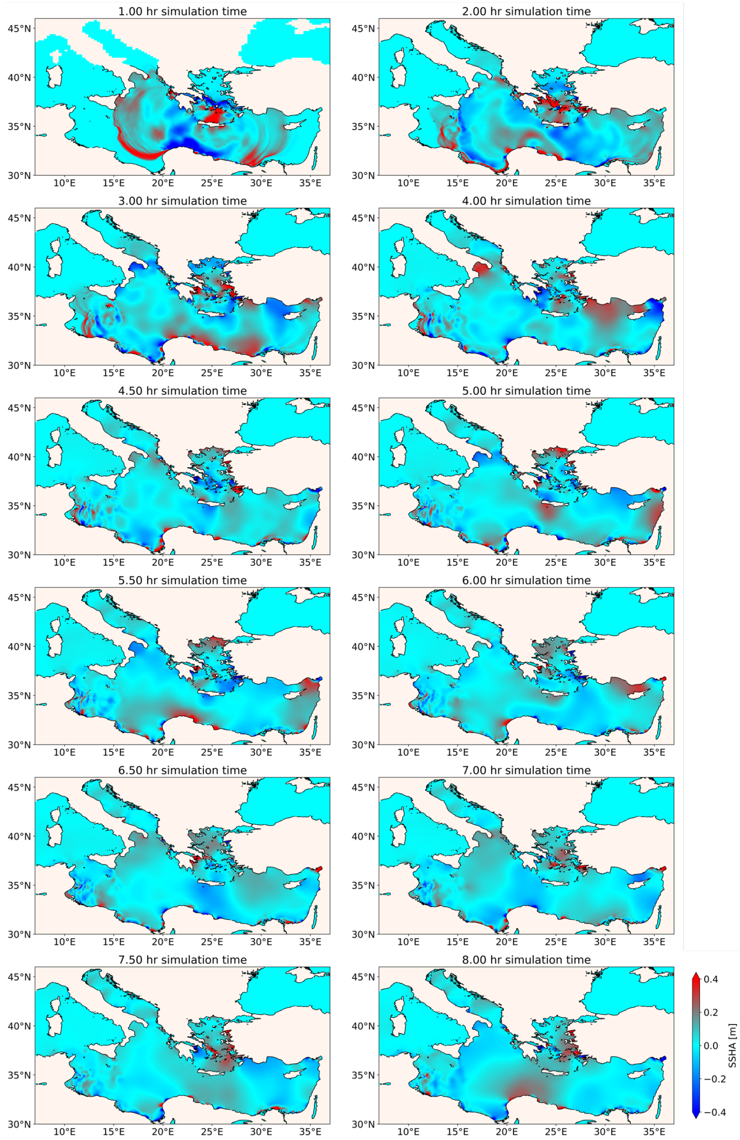

Figure C1. Tsunami evolution (ssha [m]) for model HE (eastern hypocenter) after 1 h, 2 h, 3 h, 4 h, 4.5 h, 5 h, 5.5 h, 6 h, 6.5 h, 7 h, 7.5 h, 8 h simulation time. Red marks elevation, and blue marks depression from the sea surface at rest.

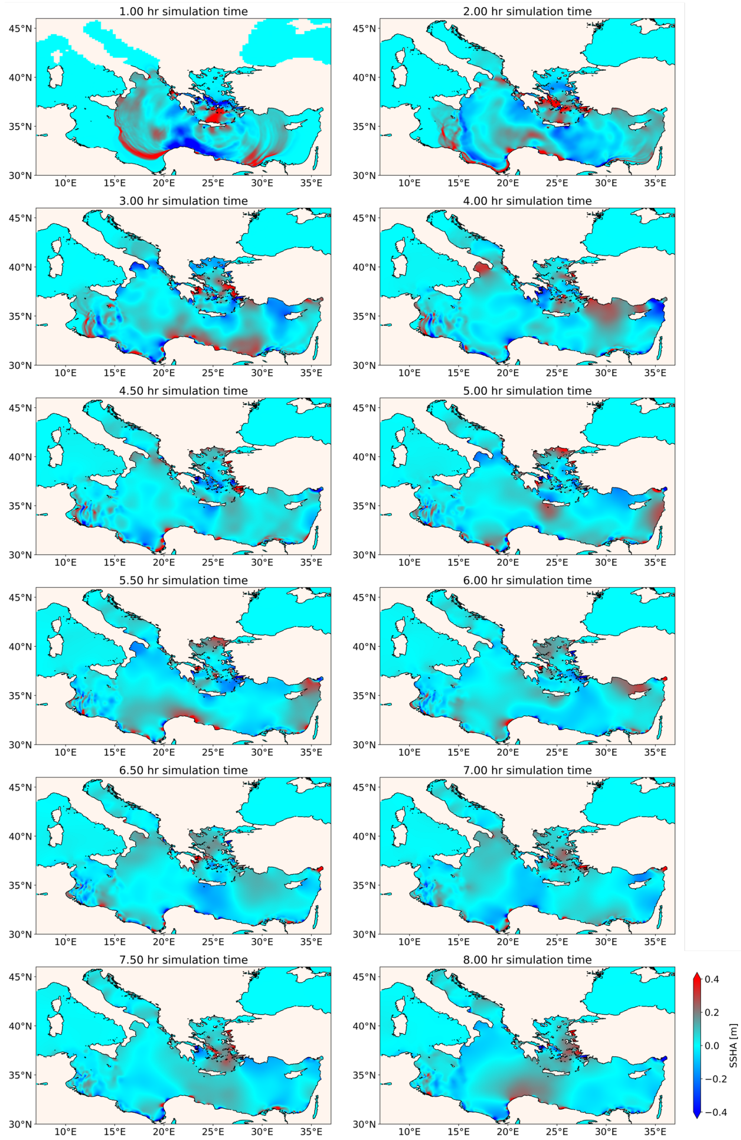

Figure C2. Tsunami evolution (ssha [m]) for model HM (middle hypocenter) after 1 h, 2 h, 3 h, 4 h, 4.5 h, 5 h, 5.5 h, 6 h, 6.5 h, 7 h, 7.5 h, 8 h simulation time. Red marks elevation, and blue marks depression from the sea surface at rest.

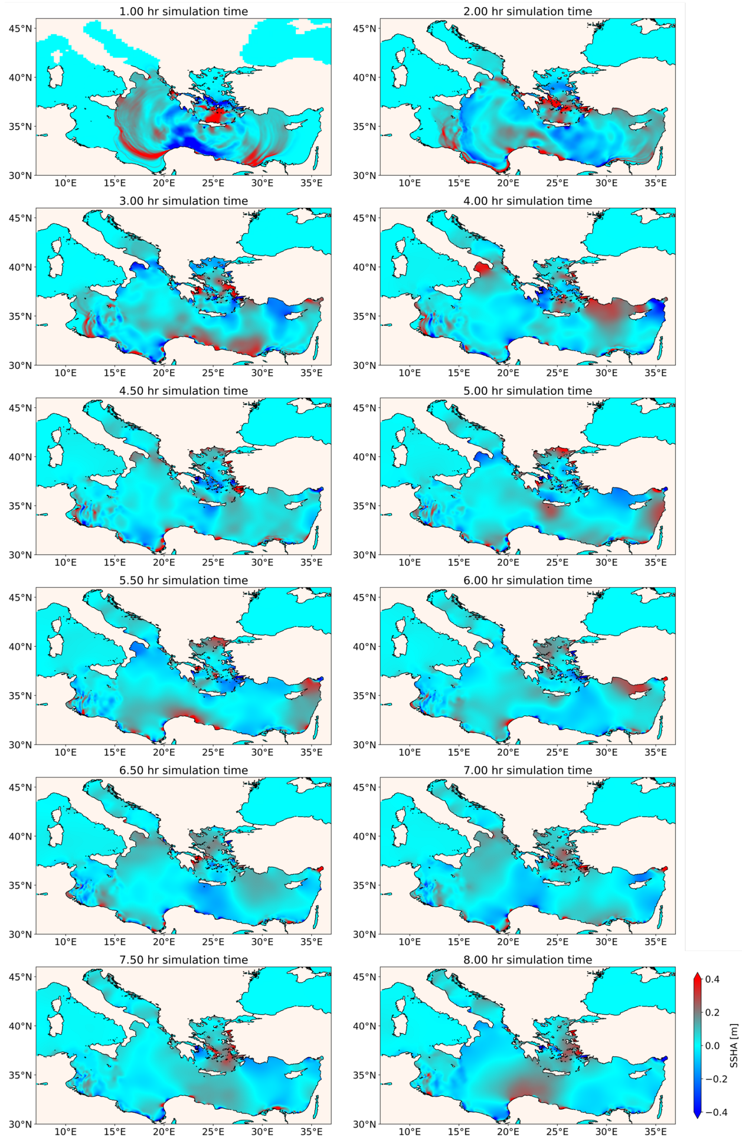

Figure C3. Tsunami evolution (ssha [m]) for model HW (western hypocenter) after 1 h, 2 h, 3 h, 4 h, 4.5 h, 5 h, 5.5 h, 6 h, 6.5 h, 7 h, 7.5 h, 8 h simulation time. Red marks elevation, and blue marks depression from the sea surface at rest.

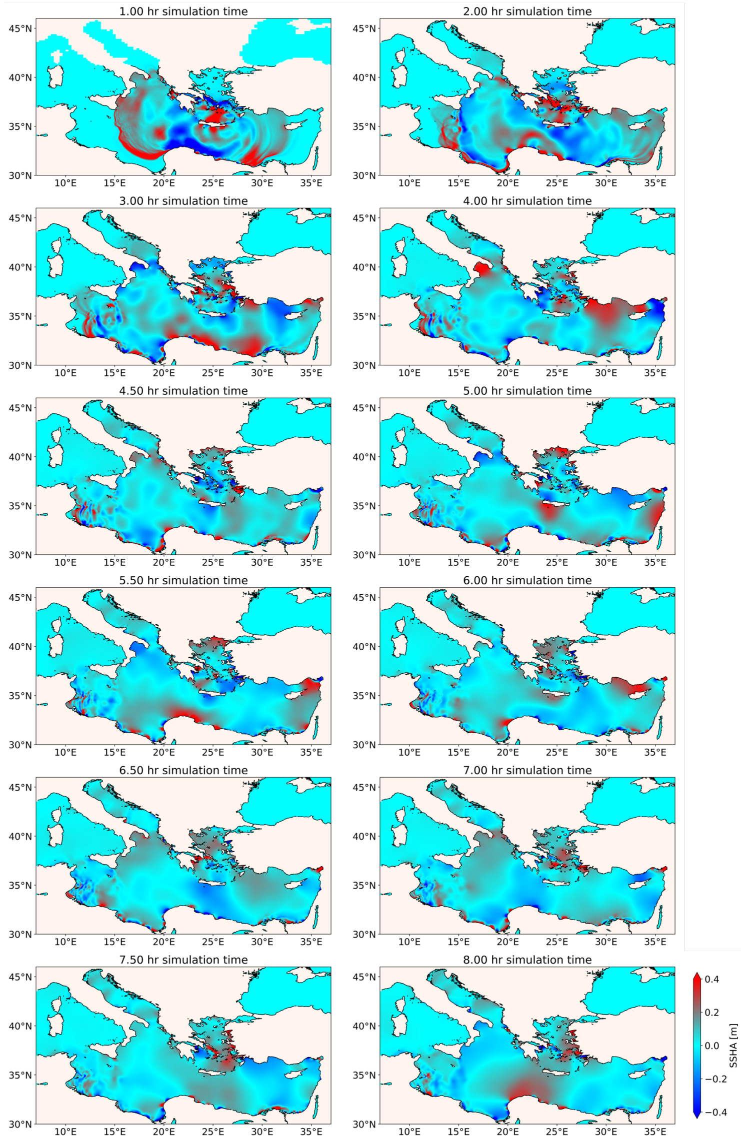

Figure C4. Tsunami evolution (ssha [m]) for model HEP (eastern hypocenter, including plastic deformation) after 1 h, 2 h, 3 h, 4 h, 4.5 h, 5 h, 5.5 h, 6 h, 6.5 h, 7 h, 7.5 h, 8 h simulation time. Red marks elevation, and blue marks depression from the sea surface at rest.

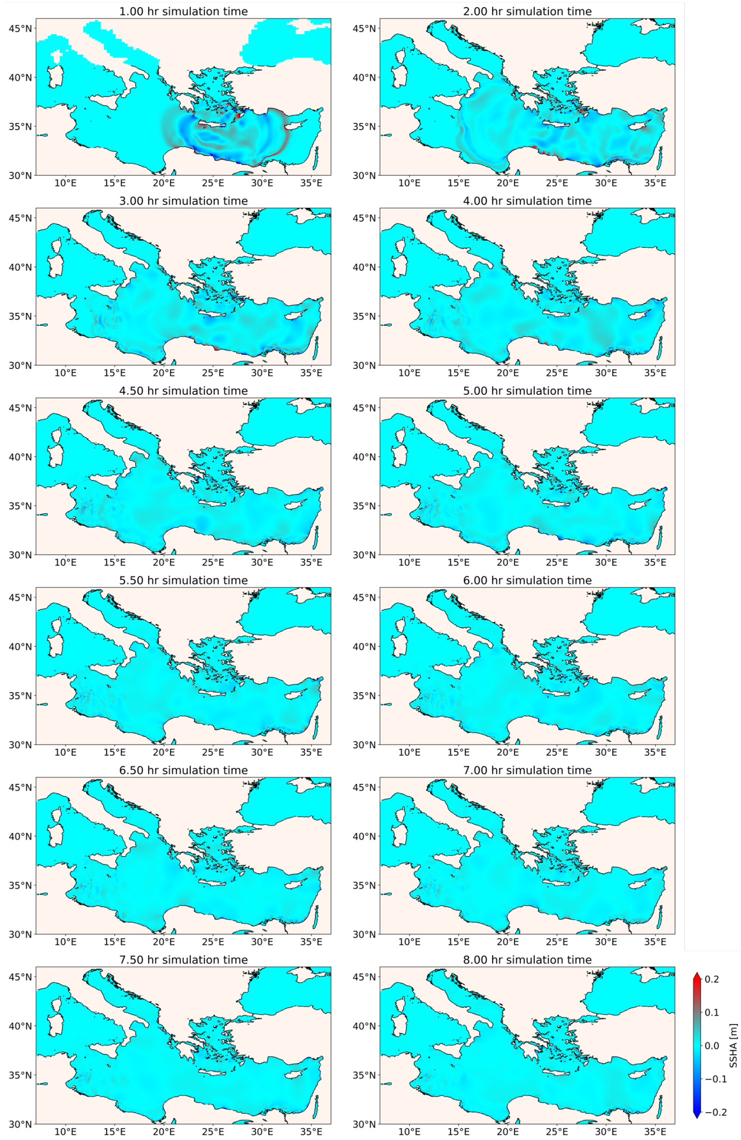

Figure C5. Tsunami evolution (ssha [m]) for model HEA (eastern hypocenter with initial stress asperity) after 1 h, 2 h, 3 h, 4 h, 4.5 h, 5 h, 5.5 h, 6 h, 6.5 h, 7 h, 7.5 h, 8 h simulation time. Red marks elevation, and blue marks depression from the sea surface at rest.

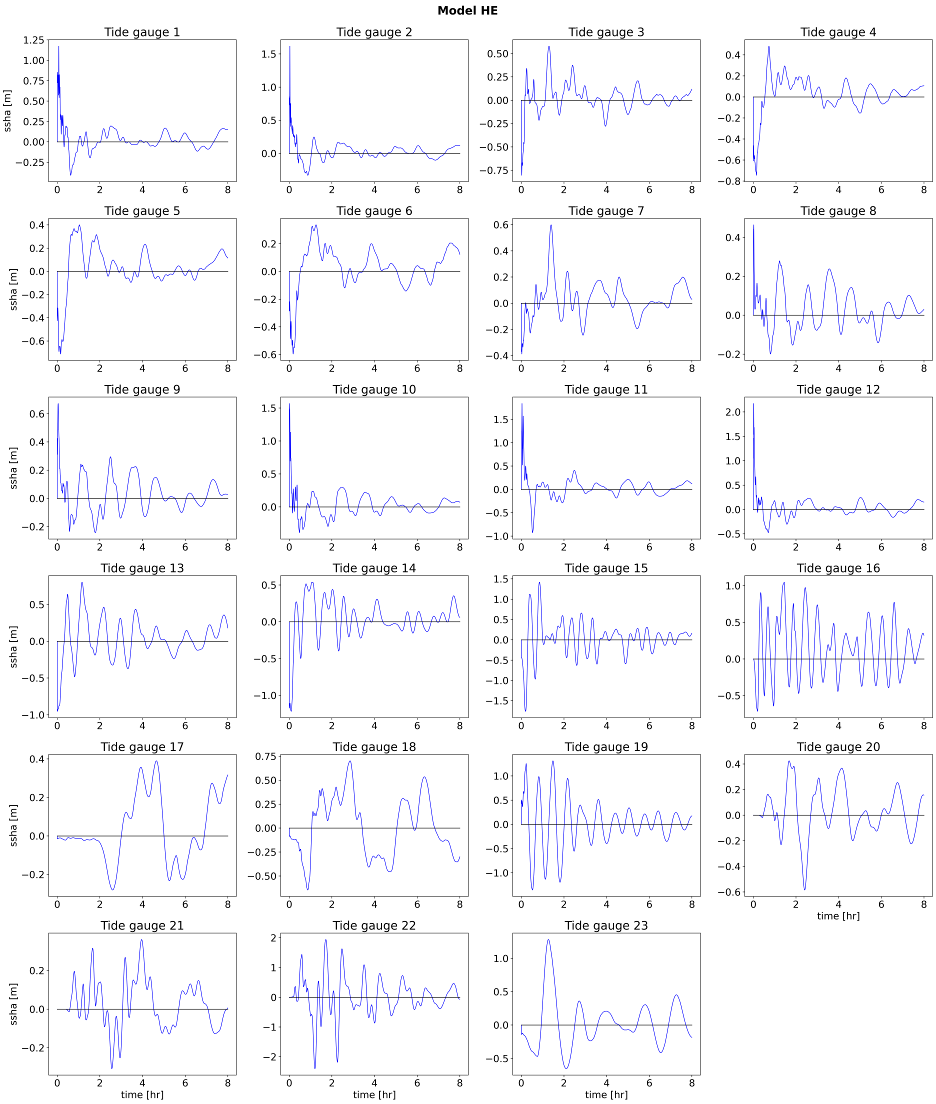

Figure C6. Synthetic tide gauges showing the sea surface height anomaly (ssha [m]) vs simulation time (8 h) for the one-way-linked model HE (eastern hypocenter) at 23 stations (Fig. 6 b).

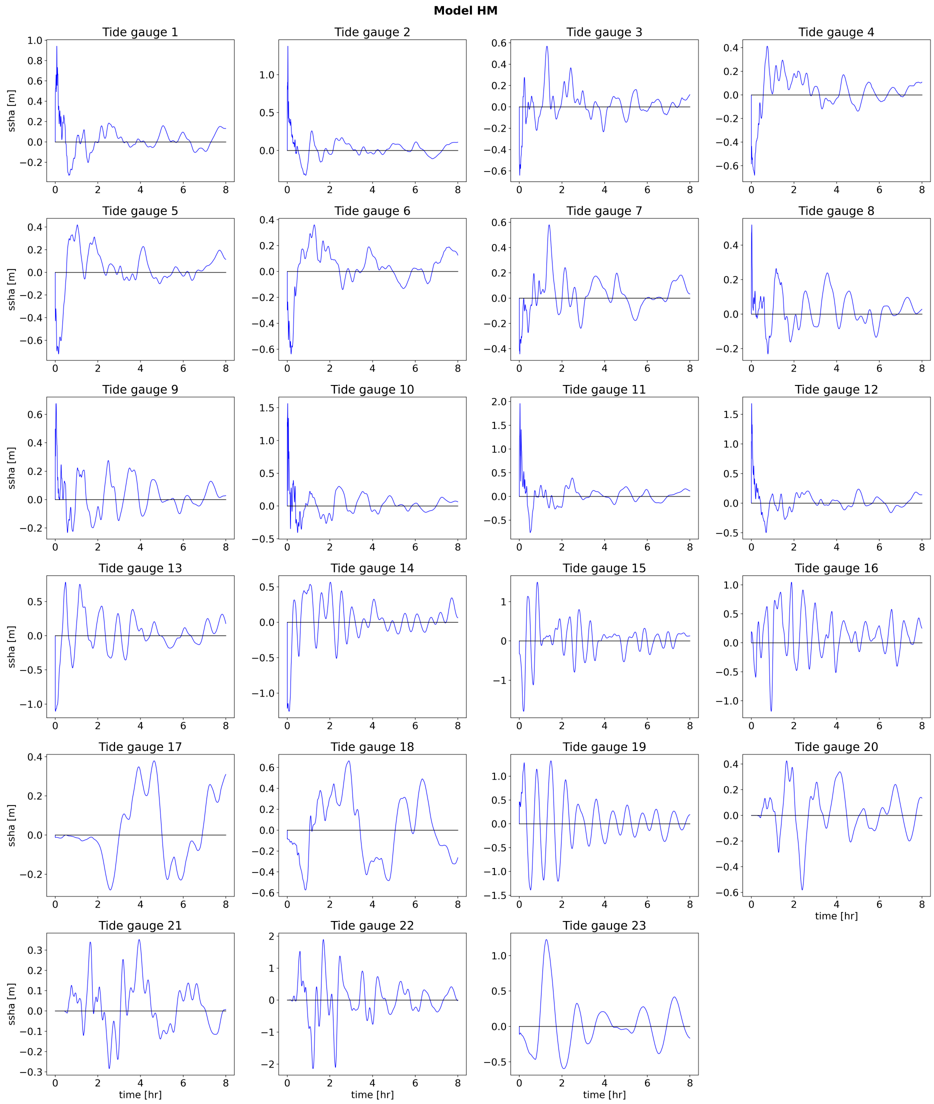

Figure C7. Synthetic tide gauges showing the sea surface height anomaly (ssha [m]) vs simulation time (8 h) for the one-way-linked model HM (middle hypocenter) at 23 stations (Fig. 6 b).

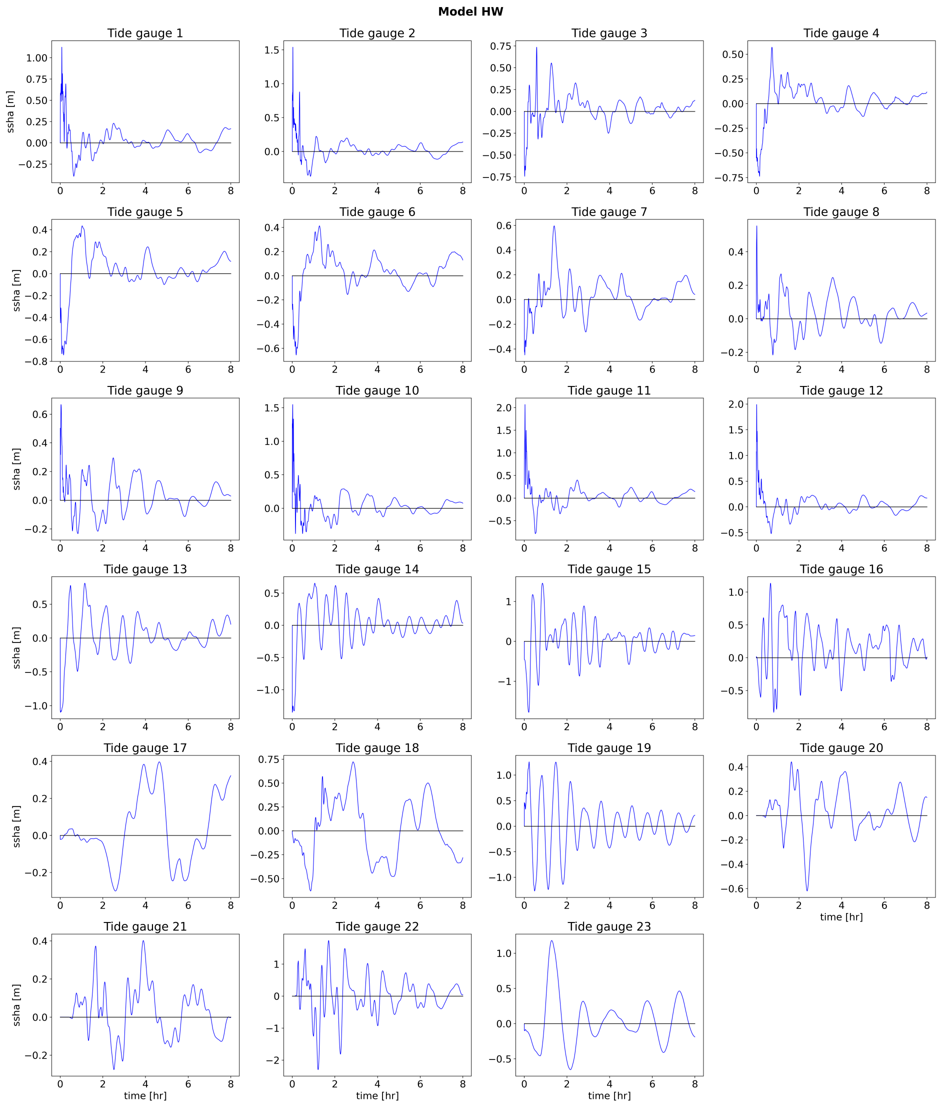

Figure C8. Synthetic tide gauges showing the sea surface height anomaly (ssha [m]) vs simulation time (8 h) for the one-way-linked model HW (western hypocenter) at 23 stations (Fig. 6 b).

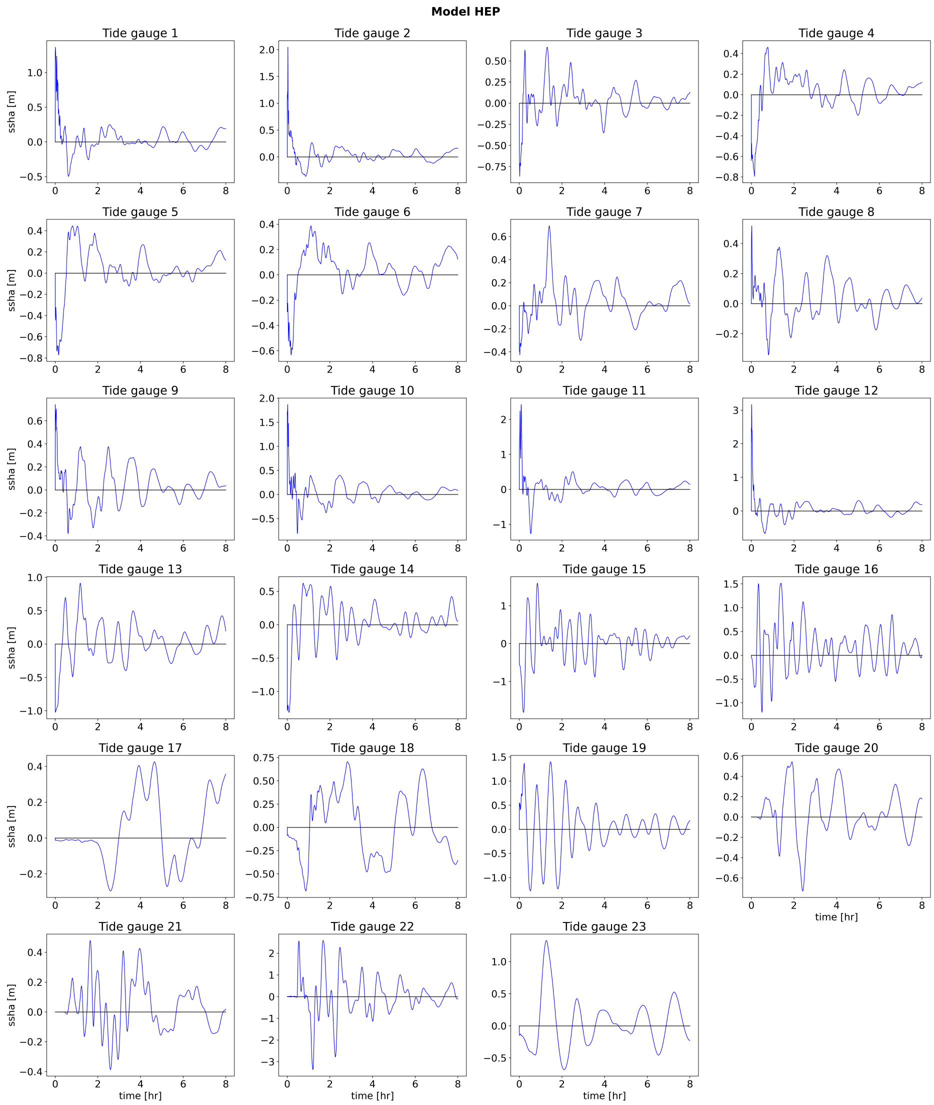

Figure C9. Synthetic tide gauges showing the sea surface height anomaly (ssha [m]) vs simulation time (8 h) for the one-way-linked model HEP (eastern hypocenter, including plastic deformation) at 23 stations (Fig. 6 b).

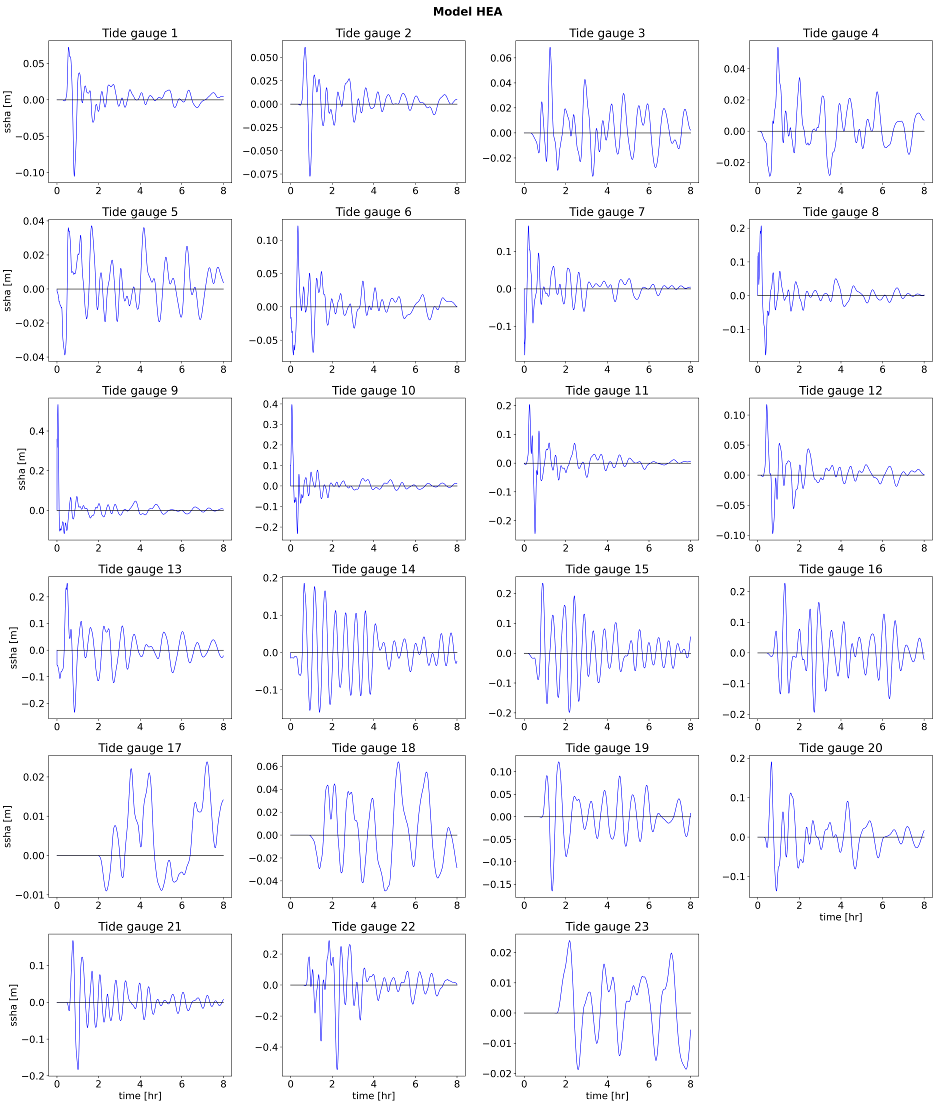

Figure C10. Synthetic tide gauges showing the sea surface height anomaly (ssha [m]) vs simulation time (8 h) for the one-way-linked model HEA (eastern hypocenter with initial stress asperity) at 23 stations (Fig. 6 b).

Appendix D Fully-coupled model: tsunami results

We here show tsunami results for the fully-coupled modeling approach after 50 s, 100 s, 200 s, 250 s, and 300 s simulation time, as well as synthetic tide gauges.

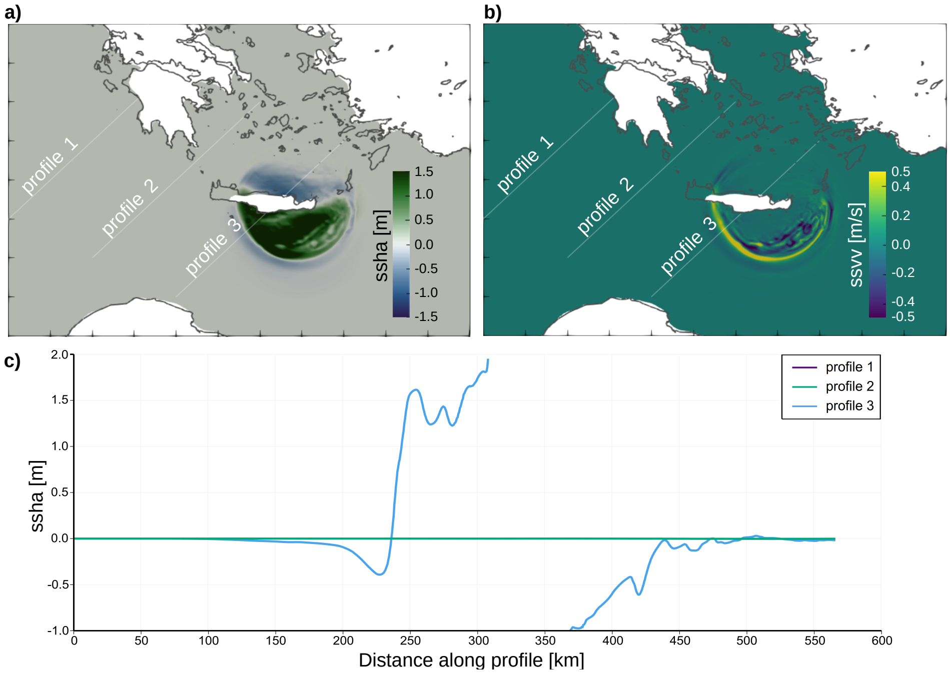

Figure D1. Results of the fully-coupled earthquake-tsunami simulation: a) ssha [m], b) ssvv [m/s], and c) cross-sections of ssha [m] after 50 s simulation time.

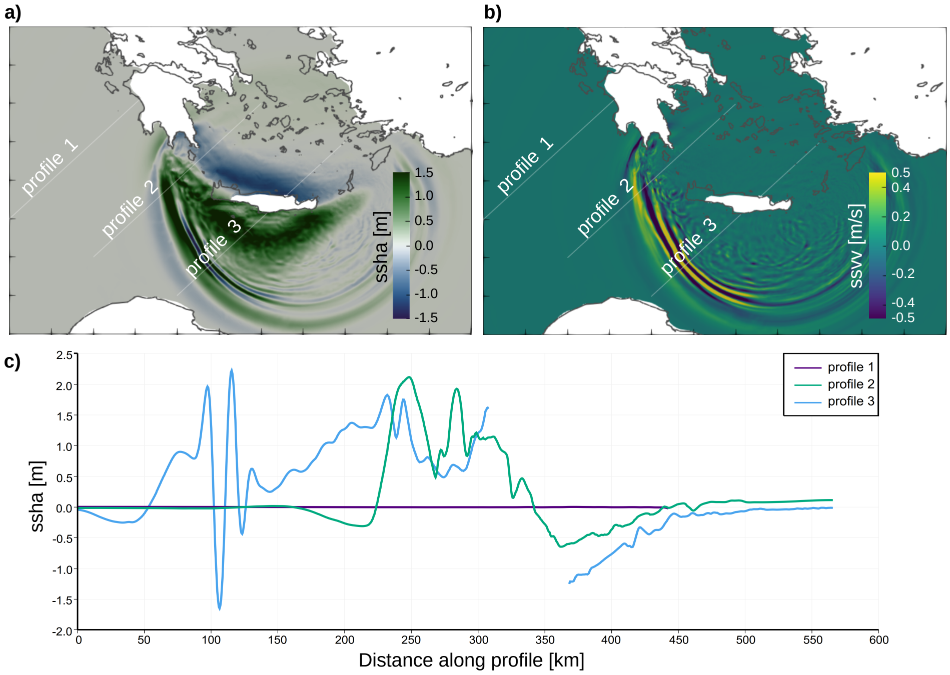

Figure D2. Results of the fully-coupled earthquake-tsunami simulation: a) ssha [m], b) ssvv [m/s], and c) cross-sections of ssha [m] after 100 s simulation time.

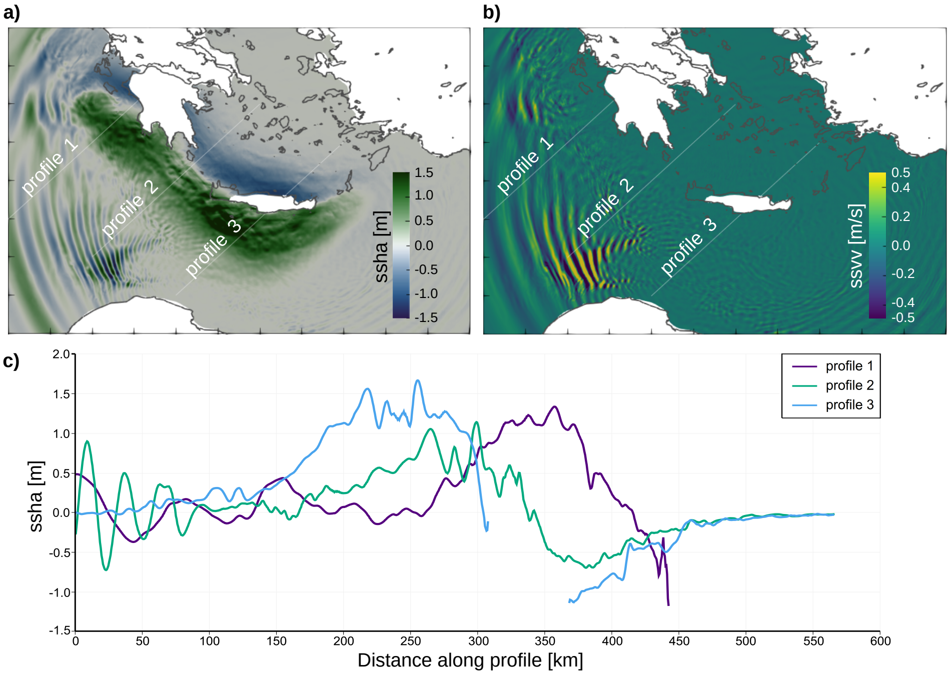

Figure D3. Results of the fully-coupled earthquake-tsunami simulation: a) ssha [m], b) ssvv [m/s], and c) cross-sections of ssha [m] after 200 s simulation time.

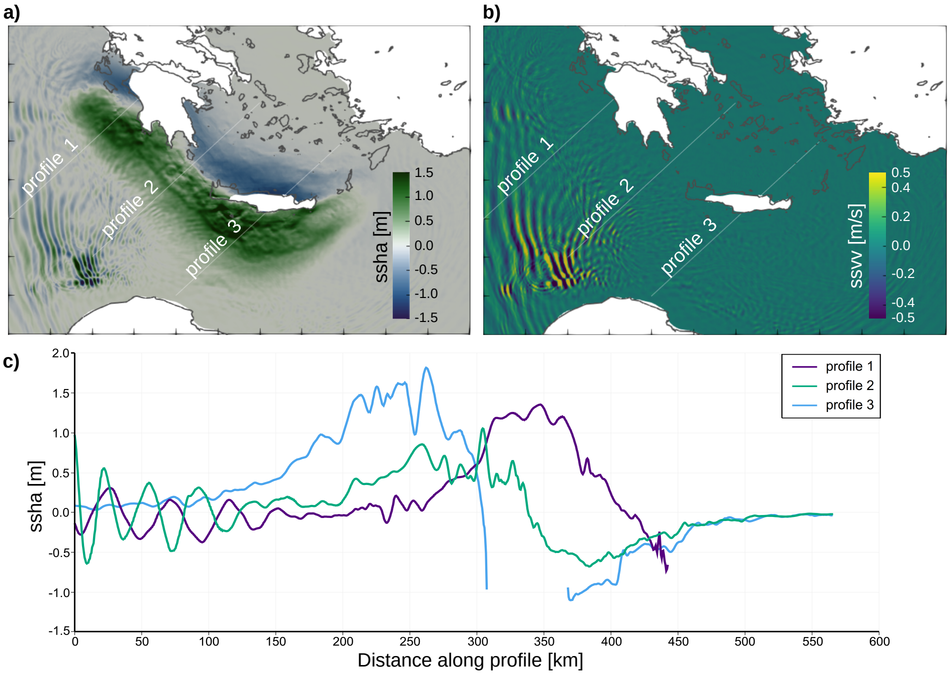

Figure D4. Results of the fully-coupled earthquake-tsunami simulation: a) ssha [m], b) ssvv [m/s], and c) cross-sections of ssha [m] after 250 s simulation time.

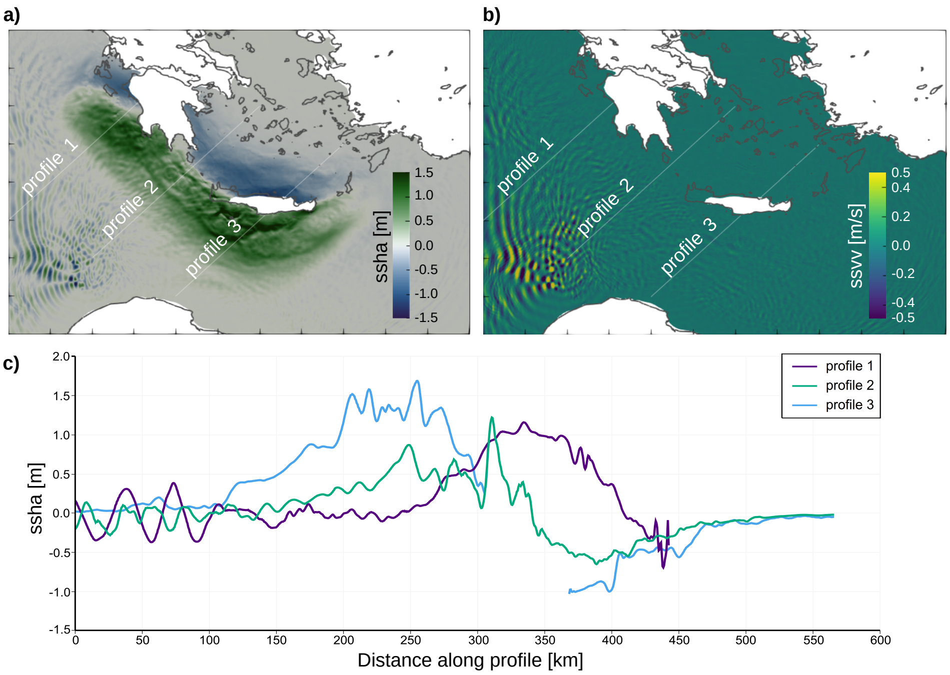

Figure D5. Results of the fully-coupled earthquake-tsunami simulation: a) ssha [m], b) ssvv [m/s], and c) cross-sections of ssha [m] after 300 s simulation time.

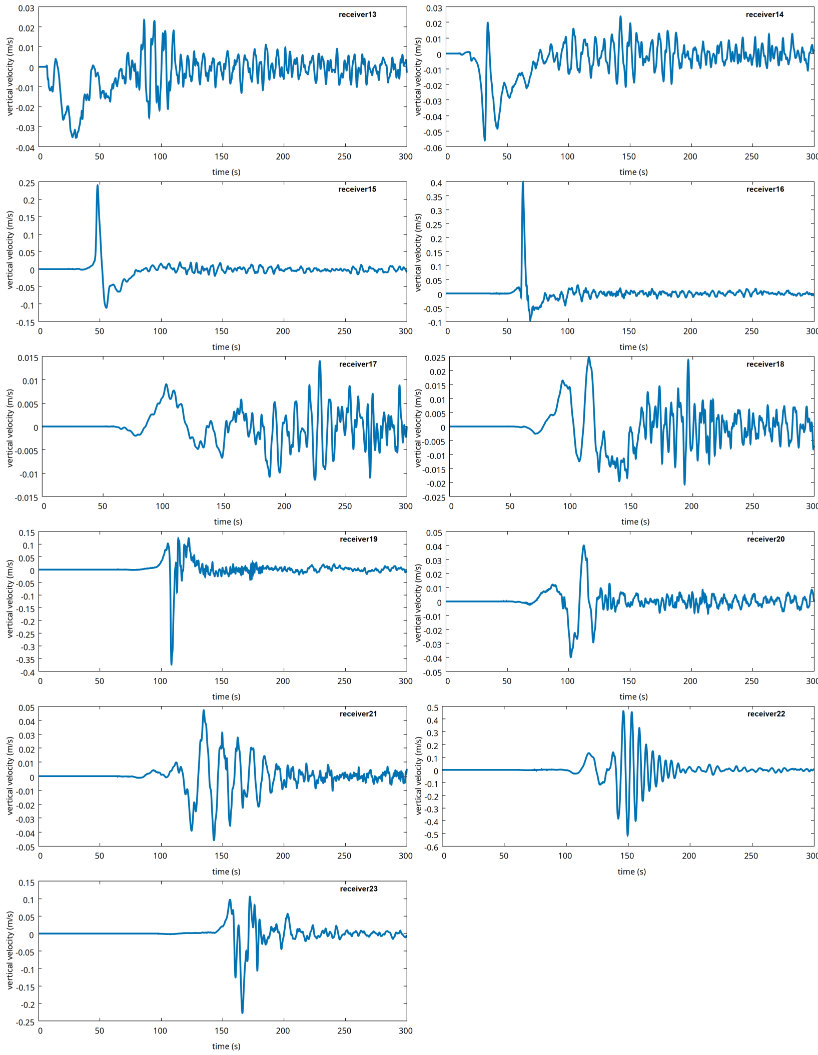

Figure D6. Synthetic tide gauges showing the sea surface vertical velocity (ssvv [m/s]) vs simulation time (300 s) for the fully-coupled earthquake-tsunami model HE (eastern hypocenter) at stations 13 to 23 (Fig. 6 b).

Conflict of Interest Statement

The authors declare that the research was conducted without any commercial or financial relationships that could be construed as a potential conflict of interest.

Acknowledgments

We thank Lukas Krenz for useful discussions, and Lauren Abrahams and Eric Dunham for their contributions to the 3D fully-coupled earthquake-tsunami modeling capabilities in SeisSol. This work received funding from the European Union's Horizon 2020 research and innovation program (TEAR ERC Starting grant agreement No. 852992) and Horizon Europe (ChEESE-2P grant No. 101093038, DT-GEO grant No. 101058129, and Geo-INQUIRE grant No. 101058518). AAG acknowledges additional support from the National Science Foundation (CRESCENT, grant no. EAR-2225286, MTMOD, grant no. EAR-2121568, CSA-LCCF, grant no. OAC-2139536, QUAKEWORX, grant no. OAC-2311208) and the National Aeronautics and Space Administration (grant no. 80NSSC20K0495). We appreciate the computing infrastructure of the Department of Earth and Environmental Sciences at LMU, Geophysics (Oeser et al., 2006). The authors gratefully acknowledge the Gauss Centre for Supercomputing e.V. (`www.gauss-centre.eu`, project pn49ha) for funding this project by providing computing time on the GCS Supercomputer SuperMUC at Leibniz Supercomputing Centre (`www.lrz.de`).

Open Research

The open-source software SeisSol (commit c25ae5d3; Uphoff et al. (2024)) has been used for dynamic rupture and fully-coupled earthquake-tsunami modeling. We used GeoClaw version 5.9.2 (Clawpack Development Team, 2023) for one-way linked tsunami simulations. SeisSol and GeoClaw are available from GitHub (`https://github.com/SeisSol`; `https://github.com/clawpack/geoclaw`; last access: 4 June 2025). We adapt the steps of Ulrich et al. (2021) for the conversion of the SeiSol output to GeoClaw input. The SeisSol and tsunami input files that are required to run the simulations, can be found here: `https://zenodo.org/records/15010623?preview=1&token=eyJhbGciOiJIUzUxMiJ9 .eyJpZCI6IjRlNjczNzViLWMzMjktNGZiMS05OWVjLTZhNjk1MTlmMTQxYyIsImRhdGEiOnt9LCJyYW5kb20iOiIwNWJjYj .i4Sj6NWCqOsSPI-Eg5A-6kXaDZvcIp6GnTDfwJ52b8BHsbmIl1kzYdP3Rd6ziahLvusi2RwExFcbWpGxl _ByBw`. We incorporate the following topography and bathymetry (GEBCO Compilation Group, 2019) at 15 arc seconds or ∼380 m resolution using the following projection: +proj=tmerc +datum=WGS84 +k=0.9996 +lon_0=24.830 +lat_0=34.790.

References

Abbate, A., Davies, G., Lorito, S., Kalligeris, N., Romano, F., Tonini, R., & Volpe, M. (2025). Importance sampling of seismic tsunami sources with near-field emphasis for inundation ptha: benchmarking with complete ensembles. *Geophysical Journal International*, *241* (1), 155–169. doi: 10.1093/gji/ggaf034

Abbate, A., González Vida, J. M., Castro Díaz, M. J., Romano, F., Bayraktar, H. B., Babeyko, A., & Lorito, S. (2024). Modelling tsunami initial conditions due to rapid coseismic seafloor displacement: efficient numerical integration and a tool to build unit source databases. *Natural Hazards and Earth System Sciences*, *24* (8), 2773–2791. doi: 10.5194/nhess-24-2773-2024

Abrahams, L. S., Krenz, L., Dunham, E. M., Gabriel, A.-A., & Saito, T. (2023). Comparison of methods for coupled earthquake and tsunami modelling. *Geophysical Journal International*, *234* (1), 404–426. doi: 10.1093/GJI/GGAD053

Ambraseys, N. (2009). *Earthquakes in the Mediterranean and Middle East: a multidisciplinary study of seismicity up to 1900* (Vol. 136). Cambridge University Press. doi: 10.1017/CBO9781139195430.004

Ambraseys, N. N. (1962). Data for the investigation of the seismic sea-waves in the Eastern Mediterranean. *Bulletin of the Seismological Society of America*, *52*, 895–913. doi: 10.1785/BSSA0520040895

Ambraseys, N. N. (1994). Material for the Investigation of the Seismicity of Libya. *Libyan Studies*, *25*, 7–22. doi: 10.1017/S0263718900006191

Amlani, F., Bhat, H. S., Simons, W. J., Schubnel, A., Vigny, C., Rosakis, A. J., ... Abidin, H. Z. (2022). Supershear shock front contribution to the tsunami from the 2018 M_W 7.5 Palu, Indonesia earthquake. *Geophysical Journal International*, *230*, 2089–2097. doi: 10.1093/GJI/GGAC162

Andrews, D. J. (1976). Rupture velocity of plane strain shear cracks. *Journal of Geophysical Research*, *81*(32), 5679–5687. doi: 10.1029/JB081I032P05679

Andrews, D. J. (2005). Rupture dynamics with energy loss outside the slip zone. *Journal of Geophysical Research: Solid Earth*, *110*(B1). doi: 10.1029/2004JB003191

Antonopoulos, J. (1980). Data from investigation on seismic sea-waves events in the Eastern Mediterranean from the birth of Christ to 500 AD. *Annals of Geophysics*, *33*, 141–161.

Aochi, H., & Madariaga, R. (2003). The 1999 Izmit, Turkey, earthquake: Nonplanar fault structure, dynamic rupture process, and strong ground motion. *Bulletin of the Seismological Society of America*, *93*(3), 1249–1266. doi: 10.1785/0120020167

Arcos, M. E. M., & LeVeque, R. J. (2015). Validating velocities in the geoclaw tsunami model using observations near hawaii from the 2011 tohoku tsunami. *Pure and Applied Geophysics*, *172*, 849–867. doi: 10.1007/s00024-014-0980-y

Baglione, E., Lorito, S., Piatanesi, A., Romano, F., Basili, R., Brizuela, B., ... Amato, A. (2021). Characterization of fault plane and coseismic slip for the 2 May 2020, Mw 6.6 Cretan Passage earthquake from tide gauge tsunami data and moment tensor solutions. *Natural Hazards and Earth System Sciences*, *21*(12), 3713–3730. doi: 10.5194/nhess-21-3713-2021

Bahrouni, N., Meghraoui, M., Bayraktar, H. B., Lorito, S., Zagrarni, M. F., Polonia, A., ... Kamoun, F. (2024). Tsunami deposits in Tunisia contemporaneous of the large 365 CE Crete earthquake and Mediterranean Sea catastrophic event. *Scientific Reports*, *14*(1), 4537. doi: 10.1038/s41598-024-53225-7

Basili, R., Brizuela, B., Herrero, A., Iqbal, S., Lorito, S., Maesano, F. E., ... Zaytsev, A. (2021). The Making of the NEAM Tsunami Hazard Model 2018 (NEAMTHM18). *Frontiers in Earth Science*, *8*. doi: 10.3389/FEART.2020.616594

Becerril, C., Sladen, A., Ampuero, J.-P., Preciado-Garbayo, J., Gonzalez-Herraez, M., Kutschera, F., ... Bouchette, F. (2025, 4). Towards tsunami early-warning with Distributed Acoustic Sensing: expected seafloor strains induced by tsunamis. *ESS Open Archive*. doi: 10.22541/essoar.174413358.84301854/v1

Benetatos, C., Kiratzi, A., Papazachos, C., & Karakaisis, G. (2004). Focal mechanisms of shallow and intermediate depth earthquakes along the hellenic arc. *Journal of Geodynamics*, *37*(2), 253–296. doi: 10.1016/j.jog.2004.02.002

Berger, M. J., George, D. L., LeVeque, R. J., & Mandli, K. T. (2011). The GeoClaw software for depth-averaged flows with adaptive refinement. *Advances in Water Resources*, *34*(9), 1195–1206. doi: 10.1016/J.ADVWATRES.2011.02.016

Bie, L., González, P. J., & Rietbrock, A. (2017). Slip distribution of the 2015 Lefkada earthquake and its implications for fault segmentation. *Geophysical Journal International*, *210*(1), 420–427. doi: 10.1093/gji/ggx171

Bird, P. (2003). An updated digital model of plate boundaries. *Geochemistry, Geophysics, Geosystems*, *4*. doi: 10.1029/2001GC000252

Bocchini, G. M., Novikova, T., Papadopoulos, G., Agalos, A., Mouzakiotis, E., Karastathis, V., & Voulgaris, N. (2020a). Tsunami potential of moderate earthquakes: The july 1, 2009 earthquake (m w 6.45) and its associated local tsunami in the hellenic arc. *Pure and Applied Geophysics*, *177*, 1315–1333.

Bocchini, G. M., Novikova, T., Papadopoulos, G., Agalos, A., Mouzakiotis, E., Karastathis, V., & Voulgaris, N. (2020b). Tsunami Potential of Moderate Earthquakes: The July 1, 2009 Earthquake (M_W 6.45) and its Associated Local Tsunami in the Hellenic Arc. *Pure and Applied Geophysics*, *177*, 1315–1333. doi: 10.1007/s00024-019-02246-9

Bohnhoff, M., Harjes, H. P., & Meier, T. (2005). Deformation and stress regimes in the Hellenic subduction zone from focal Mechanisms. *Journal of Seismology 2005 9:3*, *9*, 341–366. doi: 10.1007/S10950-005-8720-5

Bohnhoff, M., Makris, J., Papanikolaou, D., & Stavrakakis, G. (2001). Crustal investigation of the Hellenic subduction zone using wide aperture seismic data. *Tectonophysics*, *343*, 239–262. doi: 10.1016/S0040-1951(01)00264-5

Bormann, P. (2009). Global 1-D Earth models. In *New manual of seismological observatory practice (nmsop)* (pp. 1–12). Deutsches GeoForschungsZentrum GFZ.

Borrero, J. C., LeVeque, R. J., Greer, S. D., O'Neill, S., & Davis, B. N. (2015). Observations and Modelling of Tsunami Currents at the Port of Tauranga, New Zealand. In *Australasian coasts & ports conference 2015: 22nd australasian coastal and ocean engineering conference and the 15th australasian port and harbour conference.* Auckland, New Zealand: Engineers Australia and IPENZ.

Breuer, A., Heinecke, A., Rannabauer, L., & Bader, M. (2015). High-order ADER-DG minimizes energy- and time-to-solution of SeisSol. *Lecture Notes in Computer Science (including subseries Lecture Notes in Artificial Intelligence and Lecture Notes in Bioinformatics)*, *9137 LNCS*, 340–357. doi: 10.1007/978-3-319-20119-1_25

Briseid Storrøsten, E., Ragu Ramalingam, N., Lorito, S., Volpe, M., Sánchez-Linares, C., Løvholt, F., & Gibbons, S. J. (2024). Machine learning emulation of high resolution inundation maps. *Geophysical Journal International*, *238*(1), 382–399. doi: 10.1093/gji/ggae151

Byerlee, J., & Summers, R. (1976). A note on the effect of fault gouge thickness on fault stability. *International Journal of Rock Mechanics and Mining Sciences & Geomechanics Abstracts*, *13*(1), 35–36. doi: 10.1016/0148-9062(76)90226-6

Casten, U., & Snopek, K. (2006). Gravity modelling of the Hellenic subduction zone—a regional study. *Tectonophysics*, *417*(3), 183–200. doi: 10.1016/j.tecto.2005.11.002

Chen, K., Wei, G., Milliner, C., Dal Zilio, L., Liang, C., & Avouac, J.-P. (2024). Super-shear ruptures steered by pre-stress heterogeneities during the 2023 kahramanmaraş earthquake doublet. *Nature Communications*, *15*(1), 7004. doi: 10.1038/s41467-024-51446-y

Chorozoglou, D., & Papadimitriou, E. (2019). Monitoring earthquake network measures between main shocks in greece. *Journal of Seismology*, *23*, 505–519. doi: 10.1007/s10950-019-09820-7

Chousianitis, K., & Konca, A. O. (2019). Intraslab Deformation and Rupture of the Entire Subducting Crust During the 25 October 2018 Mw 6.8 Zakynthos Earthquake. *Geophysical Research Letters*, *46*(24), 14358–14367. doi: 10.1029/2019GL085845

Cifuentes-Lobos, R., Calisto, I., MacInnes, B., Moreno, M., Quezada, J., San Martín, J., ... Saavedra, C. (2023). A stochastic approach to the characterization of the seismic sources: a potential method for the assessment of sources of historical and paleo tsunami. *Stochastic Environmental Research and Risk Assessment*, *37*(7), 2399–2411. doi: 10.1007/s00477-023-02397-1

Cirella, A., Romano, F., Avallone, A., Piatanesi, A., Briole, P., Ganas, A., ... Lorito, S. (2020). The 2018 Mw 6.8 Zakynthos (Ionian Sea, Greece) earthquake: seismic source and local tsunami characterization. *Geophysical Journal International*, *221*(2), 1043–1054. doi: 10.1093/gji/ggaa053

Clawpack Development Team. (2023). *Clawpack v5.9.2* [software]. Zenodo. doi: 10.5281/zenodo.10076317

Coban, K. H., & Sayil, N. (2020). Conditional probabilities of hellenic arc earthquakes based on different distribution models. *Pure and Applied Geophysics*, *177*(11), 5133–5145. doi: 10.1007/s00024-020-02576-z

Davies, G. (2019). Tsunami variability from uncalibrated stochastic earthquake models: tests against deep ocean observations 2006–2016. *Geophysical Journal International*, *218*(3), 1939–1960. doi: 10.1093/gji/ggz260

Davies, G., Griffin, J., Løvholt, F., Glimsdal, S., Harbitz, C., Thio, H. K., ... Baptista, M. A. (2018). A global probabilistic tsunami hazard assessment from earthquake sources. *Geological Society Special Publication*, *456*, 219–244. doi: 10.1144/SP456.5

Davies, G., Weber, R., Wilson, K., & Cummins, P. (2022). From offshore to onshore probabilistic tsunami hazard assessment via efficient Monte Carlo sampling. *Geophysical Journal International*, *230*(3), 1630–1651. doi: 10.1093/gji/ggac140

De Martini, P., Barbano, M., Smedile, A., Gerardi, F., Pantosti, D., Del Carlo, P., & Pirrotta, C. (2010). A unique 4000year long geological record of multiple tsunami inundations in the Augusta Bay (eastern Sicily, Italy). *Marine Geology*, *276*(1), 42–57. doi: https://doi.org/10.1016/j.margeo.2010.07.005

de la Puente, J., Ampuero, J.-P., & Käser, M. (2009). Dynamic rupture modeling on unstructured meshes using a discontinuous galerkin method. *Journal of Geophysical Research: Solid Earth*, *114*(B10). doi: https://doi.org/10.1029/2008JB006271

Dias, F., Dutykh, D., O'Brien, L., Renzi, E., & Stefanakis, T. (2014). On the modelling of tsunami generation and tsunami inundation. *Procedia IUTAM*, *10*, 338–355. doi: 10.1016/j.piutam.2014.01.029

Dumbser, M., & Käser, M. (2006). An Arbitrary High Order Discontinuous Galerkin Method for Elastic Waves on Unstructured Meshes II: The Three-Dimensional Isotropic Case. *Geophysical Journal International*, *167*(1), 319–336. doi: 10.1111/j.1365-246X.2006.03120.x

Dunham, E. M., & Archuleta, R. J. (2005). Near-source ground motion from steady state dynamic rupture pulses. *Geophysical Research Letters*, *32*(3). doi: 10.1029/2004GL021793

Dziewonski, A. M., & Anderson, D. L. (1981). Preliminary reference Earth model. *Physics of the earth and planetary interiors*, *25*(4), 297–356.

Elbanna, A., Abdelmeguid, M., Ma, X., Amlani, F., Bhat, H. S., Synolakis, C., & Rosakis, A. J. (2021). Anatomy of Strike-Slip Fault Tsunami Genesis. *Proceedings of the National Academy of Sciences of the United States of America*, *118*(19), 2025632118. doi: 10.1073/pnas.2025632118

El-Sayed, A., Romanelli, F., & Panza, G. (2000). Recent seismicity and realistic waveforms modeling to reduce the ambiguities about the 1303 seismic activity in Egypt. *Tectonophysics*, *328*, 341–357. doi: 10.1016/S0040-1951(00)00172-4

England, P., Howell, A., Jackson, J., & Synolakis, C. (2015). Palaeotsunamis and tsunami hazards in the Eastern Mediterranean. *Philosophical Transactions of the Royal Society A: Mathematical, Physical and Engineering Sciences*, *373*. doi: 10.1098/rsta.2014.0374

Flemming, N. C. (1978). Holocene eustatic changes and coastal tectonics in the northeast Mediterranean: implications for models of crustal consumption. *Philosophical Transactions of the Royal Society of London. Series A, Mathematical and Physical Sciences*, *289*, 405–458. doi: 10.1098/RSTA.1978.0065

Folch, A., Abril, C., Afanasiev, M., Amati, G., Bader, M., Badia, R. M., ... Wössner, U. (2023). The EU Center of Excellence for Exascale in Solid Earth (ChEESE): Implementation, results, and roadmap for the second phase. *Future Generation Computer Systems*, *146*, 47–61. doi: 10.1016/j.future.2023.04.006

Galanopoulos, A. G. (1960). Tsunamis observed on the coasts of greece from antiquity to present time. *Annals of Geophysics*, *13*(3-4), 369–386.

Gallovič, F., & Valentová, L. (2023). Broadband strong ground motion modeling using planar dynamic rupture with fractal parameters. *Journal of Geophysical Research: Solid Earth*, *128*(6), e2023JB026506. doi: 10.1029/2023JB026506

Galvez, P., Dalguer, L. A., Ampuero, J., & Giardini, D. (2016). Rupture Reactivation during the 2011 Mw 9.0 Tohoku Earthquake: Dynamic Rupture and Ground-Motion Simulations. *Bulletin of the Seismological Society of America*, *106*(3), 819–831. doi: 10.1785/0120150153

Ganas, A., & Parsons, T. (2009). Three-dimensional model of Hellenic Arc deformation and origin of the Cretan uplift. *Journal of Geophysical Research: Solid Earth*, *114*, 6404. doi: 10.1029/2008JB005599

GEBCO Compilation Group. (2019). *GEBCO 2019 Grid.* doi: 10.5285/836f016a-33be-6ddc-e053-6c86abc0788e

Geist, E. L. (2002). Complex Earthquake Rupture and Local Tsunamis. *Journal of Geophysical Research: Solid Earth*, *107*(B5), ESE 2–1-ESE 2–15. doi: 10.1029/2000JB000139

Gibbons, S. J., Lorito, S., de la Asunción, M., Volpe, M., Selva, J., Macías, J., … Løvholt, F. (2022). The Sensitivity of Tsunami Impact to Earthquake Source Parameters and Manning Friction in High-Resolution Inundation Simulations. *Frontiers in Earth Science*, *9*, 1412. doi: 10.3389/feart.2021.757618

Goldsworthy, M., Jackson, J., & Haines, J. (2002). The continuity of active fault systems in Greece. *Geophysical Journal International*, *148*(3), 596–618. doi: 10.1046/j.1365-246X.2002.01609.x

Gomez, B., & Kadri, U. (2021). Near real-time calculation of submarine fault properties using an inverse model of acoustic signals. *Applied Ocean Research*, *109*, 102557. doi: 10.1016/J.APOR.2021.102557

Gonzalez, F. I., LeVeque, R. J., Chamberlain, P., Hirai, B., Varkovitzky, J., & George, D. L. (2011). Validation of the GeoClaw model. *NTHMP MMS Tsunami Inundation Model Validation Workshop*, 1–84.

Guidoboni, E., & Comastri, A. (1997). The large earthquake of 8 August 1303 in Crete: seismic scenario and tsunami in the Mediterranean area. *Journal of Seismology 1997 1:1*, *1*, 55–72. doi: 10.1023/A:1009737632542

Guidoboni, E., Comastri, A., & nazionale di geofisica e vulcanologia (Italy), I. (2005). *Catalogue of earthquakes and tsunamis in the Mediterranean area from the 11th to the 15th century.* INGV Istituto Nazionale di Geofisica e Vulcanologia.

Guidoboni, E., Traina, G., & Comastri, A. (1994). Catalogue of ancient earthquakes in the mediterranean sea up to the 10th century. *Ist. Naz. Geofis.*.

Hamouda, A. (2006). Numerical computations of 1303 tsunamigenic propagation towards alexandria, egyptian coast. *Journal of African Earth Sciences*, *44*(1), 37–44. doi: 10.1016/j.jafrearsci.2005.11.005

Harris, R. A., Aagaard, B., Barall, M., Ma, S., Roten, D., Olsen, K., … Dalguer, L. (2018). A suite of exercises for verifying dynamic earthquake rupture codes. *Seismological Research Letters*, *89*(3), 1146–1162. doi: 10.1785/0220170222

Heinecke, A., Breuer, A., Rettenberger, S., Bader, M., Gabriel, A., Pelties, C., … Dubey, P. (2014). Petascale high order dynamic rupture earthquake simulations on heterogeneous supercomputers. In *Sc '14: Proceedings of the international conference for high performance computing, networking, storage and analysis* (pp. 3–14).

Henneking, S., Venkat, S., Dobrev, V., Camier, J., Kolev, T., Fernando, M., … Ghattas, O. (2025). *Real-time Bayesian inference at extreme scale: A digital twin for tsunami early warning applied to the Cascadia subduction zone.* doi: 10.48550/arXiv.2504.16344

Ida, Y. (1972). Cohesive force across the tip of a longitudinal-shear crack and Griffith's specific surface energy. *Journal of Geophysical Research*, *77*(20), 3796–3805. doi: 10.1029/JB077I020P03796

Jongsma, D. (1977). Bathymetry and shallow structure of the Pliny and Strabo Trenches, south of the Hellenic Arc. *GSA Bulletin*, *88*(6), 797–805. doi: 10.1130/0016-7606(1977)88⟨797:BASSOT⟩2.0.CO;2

Karakostas, V. G., & Papadimitriou, E. E. (2010). Fault complexity associated with the 14 August 2003 Mw 6.2 Lefkada, Greece, aftershock sequence. *Acta geophysica*, *58*, 838–854. doi: 10.2478/s11600-010-0009-6

Kim, J., Pedersen, G. K., Løvholt, F., & LeVeque, R. J. (2017). A Boussinesq type extension of the GeoClaw model - a study of wave breaking phenomena applying dispersive long wave models. *Coastal Engineering*, *122*, 75–86. doi: 10.1016/j.coastaleng.2017.01.005

Kiratzi, A. A., & Papazachos, C. B. (1995). Active deformation on the shallow part of the subducting lithospheric slab in the southern aegean. *Journal of Geodynamics*, *19*(1), 65–78. doi: 10.1016/0264-3707(94)E0002-C

Kozdon, J. E., & Dunham, E. M. (2014). Constraining shallow slip and tsunami excitation in megathrust ruptures using seismic and ocean acoustic waves recorded on ocean-bottom sensor networks. *Earth and Planetary Science Letters*, *396*, 56–65. doi: 10.1016/j.epsl.2014.04.001

Kreemer, C., & Chamot-Rooke, N. (2004). Contemporary kinematics of the southern Aegean and the Mediterranean Ridge. *Geophysical Journal International*, *157*(3), 1377–1392. doi: 10.1111/j.1365-246X.2004.02270.x

Krenz, L., Uphoff, C., Ulrich, T., Gabriel, A. A., Abrahams, L. S., Dunham, E. M., & Bader, M. (2021). 3D Acoustic-Elastic Coupling with Gravity: The Dynamics of the 2018 Palu, Sulawesi Earthquake and Tsunami. *International Conference for High Performance Computing, Networking, Storage and Analysis, SC*. doi: 10.1145/3458817.3476173

Kutschera, F., Gabriel, A.-A., Wirp, S. A., Li, B., Ulrich, T., Abril, C., & Halldórsson, B. (2024). Linked and fully coupled 3D earthquake dynamic rupture and tsunami modeling for the Húsavík–Flatey Fault Zone in North Iceland. *Solid Earth*, *15*(2), 251–280. doi: 10.5194/se-15-251-2024

Kutschera, F., Jia, Z., Oryan, B., Wong, J. W. C., Fan, W., & Gabriel, A.-A. (2024). The Multi-Segment Complexity of the 2024 Mw 7.5 Noto Peninsula Earthquake Governs Tsunami Generation. *Geophysical Research Letters*, *51*(21), e2024GL109790. doi: 10.1029/2024GL109790

Käser, M., & Dumbser, M. (2006). An arbitrary high-order discontinuous Galerkin method for elastic waves on unstructured meshes - I. The two-dimensional isotropic case with external source terms. *Geophysical Journal International*, *166*(2), 855–877. doi: 10.1111/j.1365-246X.2006.03051.x

Laigle, M., Sachpazi, M., & Hirn, A. (2004). Variation of seismic coupling with slab detachment and upper plate structure along the western Hellenic subduction zone. *Tectonophysics*, *391*, 85–95. doi: 10.1016/J.TECTO.2004.07.009

Lambert, V., Lapusta, N., & Faulkner, D. (2021). Scale dependence of earthquake rupture prestress in models with enhanced weakening: Implications for event statistics and inferences of fault stress. *Journal of Geophysical Research: Solid Earth*, *126*(10), e2021JB021886. doi: 10.1029/2021JB021886

Le Pichon, X., & Angelier, J. (1981). The Aegean Sea. *Philosophical Transactions of the Royal Society of London. Series A, Mathematical and Physical Sciences*, *300*(1454), 357–372. doi: 10.1098/rsta.1981.0069

LeVeque, R. J., & George, D. L. (2008). High-Resolution Finite Volume Methods for the Shallow Water Equations With Bathymetry and Dry States. *Advanced Numerical Models for Simulating Tsunami Waves and Runup*, 43–73. doi: 10.1142/9789812790910_0002

LeVeque, R. J., George, D. L., & Berger, M. J. (2011). Tsunami modelling with adaptively refined finite volume methods. *Acta Numerica*, *20*, 211–289. doi: 10

.1017/S0962492911000043

Li, B., Gabriel, A.-A., Ulrich, T., Abril, C., & Halldorsson, B. (2023). Dynamic Rupture Models, Fault Interaction and Ground Motion Simulations for the Segmented Húsavík-Flatey Fault Zone, Northern Iceland. *Journal of Geophysical Research: Solid Earth*, *128*(6), e2022JB025886. doi: 10.1029/2022JB025886

Lorito, S., Selva, J., Basili, R., Romano, F., Tiberti, M. M., & Piatanesi, A. (2015). Probabilistic hazard for seismically induced tsunamis: accuracy and feasibility of inundation maps. *Geophysical Journal International*, *200*, 574–588. doi: 10.1093/GJI/GGU408

Lotto, G. C., & Dunham, E. M. (2015). High-order finite difference modeling of tsunami generation in a compressible ocean from offshore earthquakes. *Computational Geosciences*, *19*(2), 327–340. doi: 10.1007/S10596-015-9472-0

Lotto, G. C., Dunham, E. M., Jeppson, T. N., & Tobin, H. J. (2017). The effect of compliant prisms on subduction zone earthquakes and tsunamis. *Earth and Planetary Science Letters*, *458*, 213–222. doi: 10.1016/J.EPSL.2016.10.050

Lotto, G. C., Jeppson, T. N., & Dunham, E. M. (2018). Fully Coupled Simulations of Megathrust Earthquakes and Tsunamis in the Japan Trench, Nankai Trough, and Cascadia Subduction Zone. *Pure and Applied Geophysics*, *176*(9), 4009–4041. doi: 10.1007/S00024-018-1990-Y

Lund, B., & Townend, J. (2007). Calculating horizontal stress orientations with full or partial knowledge of the tectonic stress tensor. *Geophysical Journal International*, *170*(3), 1328–1335. doi: 10.1111/j.1365-246X.2007.03468.x

Luo, Y., & Liu, Z. (2021). Fault zone heterogeneities explain depth-dependent pattern and evolution of slow earthquakes in Cascadia. *Nature Communications*, *12*(1), 1959. doi: 10.1038/s41467-021-22232-x

Ma, S. (2008). A physical model for widespread near-surface and fault zone damage induced by earthquakes. *Geochemistry, Geophysics, Geosystems*, *9*(11). doi: 10.1029/2008GC002231

Ma, S. (2022). Dynamic off-fault failure and tsunamigenesis at strike-slip restraining bends: Fully-coupled models of dynamic rupture, ocean acoustic waves, and tsunami in a shallow bay. *Tectonophysics*, *838*, 229496. doi: 10.1016/J.TECTO.2022.229496

Ma, S., & Nie, S. (2019). Dynamic Wedge Failure and Along-Arc Variations of Tsunamigenesis in the Japan Trench Margin. *Geophysical Research Letters*, *46*(15), 8782–8790. doi: 10.1029/2019GL083148

Macías, J., Castro, M. J., Ortega, S., Escalante, C., & González-Vida, J. M. (2017). Performance benchmarking of tsunami-HySEA model for NTHMP's inundation mapping activities. *Pure and Applied Geophysics*, *174*, 3147–3183. doi: 10.1007/s00024-017-1583-1

MacInnes, B. T., Gusman, A. R., LeVeque, R. J., & Tanioka, Y. (2013). Comparison of earthquake source models for the 2011 tohoku event using tsunami simulations and near-field observations. *Bulletin of the Seismological Society of America*, *103*(2B), 1256–1274. doi: 10.1785/0120120121

Madden, E. H., Bader, M., Behrens, J., Dinther, Y. V., Gabriel, A. A., Rannabauer, L., … Zelst, I. V. (2020). Linked 3-D modelling of megathrust earthquake-tsunami events: from subduction to tsunami run up. *Geophysical Journal International*, *224*, 487–516. doi: 10.1093/GJI/GGAA484

Maeda, T., Furumura, T., Noguchi, S., Takemura, S., Sakai, S., Shinohara, M., … Lee, S. J. (2013). Seismic- and Tsunami-Wave Propagation of the 2011 Off the Pacific Coast of Tohoku Earthquake as Inferred from the Tsunami-Coupled Finite-Difference Simulation. *Bulletin of the Seismological Society of America*, *103*(2B), 1456–1472. doi: 10.1785/0120120118

McClusky, S., Balassanian, S., Barka, A., Demir, C., Ergintav, S., Georgiev, I., … Veis, G. (2000). Global Positioning System constraints on plate kinematics and dynamics in the eastern Mediterranean and Caucasus. *Journal of Geophysical*

Research: Solid Earth, *105*, 5695–5719. doi: 10.1029/1999JB900351

McClusky, S., Reilinger, R., Mahmoud, S., Ben Sari, D., & Tealeb, A. (2003). GPS constraints on Africa (Nubia) and Arabia plate motions. *Geophysical Journal International*, *155*(1), 126–138. doi: 10.1046/j.1365-246X.2003.02023.x

McKenzie, D. (1972). Active Tectonics of the Mediterranean Region. *Geophysical Journal International*, *30*(2), 109–185. doi: 10.1111/j.1365-246X.1972.tb02351.x

McKenzie, D. (1978). Active tectonics of the Alpine—Himalayan belt: the Aegean Sea and surrounding regions. *Geophysical Journal International*, *55*(1), 217–254. doi: 10.1111/J.1365-246X.1978.TB04759.X

Mei, C. C., & Kadri, U. (2017). Sound signals of tsunamis from a slender fault. *Journal of Fluid Mechanics*, *836*, 352–373. doi: 10.1017/JFM.2017.811

Melgar, D. (2025). *Consideration of rupture kinematics increases tsunami amplitudes in far-field hazards assessments.* EarthArXiv. doi: 10.31223/X5BQ61

Melgar, D., & Bock, Y. (2013). Near-field tsunami models with rapid earthquake source inversions from land- and ocean-based observations: The potential for forecast and warning. *Journal of Geophysical Research: Solid Earth*, *118*(11), 5939–5955. doi: https://doi.org/10.1002/2013JB010506

Meng, J., Sinoplu, O., Zhou, Z., Tokay, B., Kusky, T., Bozkurt, E., & Wang, L. (2021). Greece and Turkey shaken by African tectonic retreat. *Scientific Reports*, *11*(1), 6486.

Mohammad, H., & Riadi, G. A. (2021). Source modeling and spectral analysis of the Crete tsunami of 2nd May 2020 along the Hellenic Subduction Zone, offshore Greece. *Earth, Planets and Space (Online)*, *73*(1). doi: 10.1186/s40623-021-01394-4

Mori, N., Mai, P. M., Goda, K., & Yasuda, T. (2017). Tsunami inundation variability from stochastic rupture scenarios: Application to multiple inversions of the 2011 tohoku, japan earthquake. *Coastal Engineering*, *127*, 88–105. doi: https://doi.org/10.1016/j.coastaleng.2017.06.013

Murphy, S., Scala, A., Herrero, A., Lorito, S., Festa, G., Trasatti, E., ... Nielsen, S. (2016). Shallow slip amplification and enhanced tsunami hazard unravelled by dynamic simulations of mega-thrust earthquakes. *Scientific Reports 2016 6:1*, *6*, 1–12. doi: 10.1038/srep35007

Noguchi, S., Maeda, T., & Furumura, T. (2013, 1). FDM Simulation of an Anomalous Later Phase from the Japan Trench Subduction Zone Earthquakes. *Pure and Applied Geophysics*, *170*(1-2), 95–108. (Publisher: Birkhauser Verlag AG) doi: 10.1007/S00024-011-0412-1/METRICS

Oeser, J., Bunge, H. P., & Mohr, M. (2006). Cluster Design in the Earth Sciences Tethys. *Lecture Notes in Computer Science (including subseries Lecture Notes in Artificial Intelligence and Lecture Notes in Bioinformatics)*, *4208 LNCS*, 31–40. doi: 10.1007/11847366_4

Okal, E. A., Synolakis, C. E., Uslu, B., Kalligeris, N., & Voukouvalas, E. (2009). The 1956 earthquake and tsunami in Amorgos, Greece. *Geophysical Journal International*, *178*(3), 1533–1554. doi: 10.1111/j.1365-246X.2009.04237.x

Oliver, J., & Major, M. (1960). Leaking modes and the PL phase. *Bulletin of the Seismological Society of America*, *50*(2), 165–180. doi: 10.1785/BSSA0500020165

Omira, R., Ramalho, R. S., Kim, J., González, P. J., Kadri, U., Miranda, J. M., ... Baptista, M. A. (2022). Global Tonga tsunami explained by a fast-moving atmospheric source. *Nature*, *609*(7928), 734–740. doi: 10.1038/s41586-022-04926-4

Ozer, C., Gok, E., & Polat, O. (2018). Three-Dimensional Seismic Velocity Structure of the Aegean Region of Turkey from Local Earthquake Tomography. *Annals of Geophysics*, *61*(1), SE111. doi: 10.4401/ag-7543

Panzera, F., Zechar, J. D., Vogfjörd, K. S., & Eberhard, D. A. (2016). A revised earthquake catalogue for South Iceland. *Pure and Applied Geophysics*, *173*, 97–116. doi: 10.1007/s00024-015-1115-9

Papadimitriou, E., Karakostas, V., Mesimeri, M., & Vallianatos, F. (2016). The Mw6.7 12 October 2013 western Hellenic Arc main shock and its aftershock sequence: implications for the slab properties. *International Journal of Earth Sciences*, *105*, 2149–2160. doi: 10.1007/s00531-016-1294-3

Papadimitriou, E. E., & Karakostas, V. G. (2008). Rupture model of the great AD 365 Crete earthquake in the southwestern part of the Hellenic Arc. *Acta Geophysica*, *56*, 293–312. doi: 10.2478/s11600-008-0001-6

Papadopoulos, G., & Chalkis, B. (1984). Tsunamis observed in greece and the surrounding area from antiquity up to the present times. *Marine Geology*, *56*(1-4), 309–317.

Papadopoulos, G., Minoura, K., Imamura, F., Kuran, U., Yalçiner, A., Fokaefs, A., & Takahashi, T. (2012). Geological evidence of tsunamis and earthquakes at the Eastern Hellenic Arc: correlation with historical seismicity in the eastern Mediterranean Sea. *Research in Geophysics*, *2*, 12. doi: 10.4081/rg.2012.e12

Papadopoulos, G. A., Agalos, A., Minadakis, G., Triantafyllou, I., & Krassakis, P. (2020). Short-term foreshocks as key information for mainshock timing and rupture: The Mw6.8 25 October 2018 Zakynthos earthquake, Hellenic subduction zone. *Sensors*, *20*(19). doi: 10.3390/s20195681

Papadopoulos, G. A., Daskalaki, E., Fokaefs, A., & Giraleas, N. (2010). Tsunami hazard in the Eastern Mediterranean Sea: Strong earthquake and tsunamis in the West Hellenic Arc and trench system. *Journal of Earthquake and Tsunami*, *04*(03), 145–179. doi: 10.1142/S1793431110000856

Papadopoulos, G. A., Karastathis, V. K., Koukouvelas, I., Sachpazi, M., Baskoutas, I., Chouliaras, G., … Triantafyllou, I. (2014). The Cephalonia, Ionian Sea (Greece), sequence of strong earthquakes of January-February 2014: a first report. *Research in Geophysics*, *4*(1). doi: 10.4081/rg.2014.5441

Papadopoulos, G. A., & Kijko, A. (1991). Maximum likelihood estimation of earthquake hazard parameters in the aegean area from mixed data. *Tectonophysics*, *185*(3), 277–294. doi: https://doi.org/10.1016/0040-1951(91)90449-3

Papadopoulos, G. A., Lekkas, E., Katsetsiadou, K.-N., Rovythakis, E., & Yahav, A. (2020). Tsunami Alert Efficiency in the Eastern Mediterranean Sea: The 2 May 2020 Earthquake (Mw6.6) and near-field tsunami south of Crete (Greece). *GeoHazards*, *1*(1), 44–60. doi: 10.3390/geohazards1010005

Papadopoulos, N., & Chatziathanasiou, S. (2011). Ert pollution monitoring in areas of olive oil mills' wastes (oomw): Preliminary results from a disposal site in crete (greece). *Berichte Geol. B.-A*, *93*, 193–197.

Papazachos, B., & Papazachou, C. (2003). The earthquakes of greece, ziti publ. *Co., Thessaloniki, Greece*.

Papazachos, C. B., & Kiratzi, A. A. (1996). A detailed study of the active crustal deformation in the aegean and surrounding area. *Tectonophysics*, *253*(1), 129–153. doi: 10.1016/0040-1951(95)00047-X

Pelties, C., Gabriel, A.-A., & Ampuero, J.-P. (2014). Verification of an ADER-DG method for complex dynamic rupture problems. *Geoscientific Model Development*, *7*(3), 847–866. doi: 10.5194/gmd-7-847-2014

Pichon, X. L., & Angelier, J. (1979). The hellenic arc and trench system: A key to the neotectonic evolution of the eastern mediterranean area. *Tectonophysics*, *60*(1), 1–42. doi: 10.1016/0040-1951(79)90131-8

Pirazzoli, P. A., Ausseil-Badie, J., Giresse, P., Hadjidaki, E., & Arnold, M. (1992). Historical environmental changes at phalasarna harbor, West Crete. *Geoarchaeology*, *7*, 371–392. doi: 10.1002/GEA.3340070406

Pirazzoli, P. A., Laborel, J., & Stiros, S. C. (1996). Earthquake clustering in the Eastern Mediterranean during historical times. *J. Geophys. Res.*, *101*, 6083–6097. doi: 10.1029/95jb00914

Pirazzoli, P. A., Thommeret, J., Thommeret, Y., Laborel, J., & Montag-Gioni, L. F. (1982). Crustal block movements from Holocene shorelines: Crete and Antikithera (Greece). *Tectonophysics*, *86*, 27–43. doi: 10.1016/0040-1951(82)90060-9

Prada, M., Galvez, P., Ampuero, J.-P., Sallarès, V., Sánchez-Linares, C., Macías, J., & Peter, D. (2021). The influence of depth-varying elastic properties of the upper plate on megathrust earthquake rupture dynamics and tsunamigenesis. *Journal of Geophysical Research: Solid Earth*, *126*(11), e2021JB022328. doi: 10.1029/2021JB022328

Reilinger, R., McClusky, S., Vernant, P., Lawrence, S., Ergintav, S., Cakmak, R., … Karam, G. (2006). GPS constraints on continental deformation in the Africa-Arabia-Eurasia continental collision zone and implications for the dynamics of plate interactions. *Journal of Geophysical Research: Solid Earth*, *111*. doi: 10.1029/2005JB004051

Ripperger, J., Mai, P. M., & Ampuero, J.-P. (2008). Variability of near-field ground motion from dynamic earthquake rupture simulations. *Bulletin of the Seismological Society of America*, *98*(3), 1207–1228. doi: 10.1785/0120070076

Sachpazi, M., Laigle, M., Charalampakis, M., Diaz, J., Kissling, E., Gesret, A., … Hirn, A. (2016). Segmented hellenic slab rollback driving aegean deformation and seismicity. *Geophysical Research Letters*, *43*(2), 651–658. doi: https://doi.org/10.1002/2015GL066818

Saito, T., Baba, T., Inazu, D., Takemura, S., & Fukuyama, E. (2019). Synthesizing sea surface height change including seismic waves and tsunami using a dynamic rupture scenario of anticipated Nankai trough earthquakes. *Tectonophysics*, *769*, 228166. doi: 10.1016/J.TECTO.2019.228166

Savran, W. H., & Olsen, K. B. (2020). Kinematic Rupture Generator Based on 3-D Spontaneous Rupture Simulations Along Geometrically Rough Faults. *Journal of Geophysical Research: Solid Earth*, *125*(10), e2020JB019464. doi: 10.1029/2020JB019464

Scala, A., Lorito, S., Escalante Sánchez, C., Romano, F., Festa, G., Abbate, A., … Gonzalez-Vida, J. M. (2024). Assessing the optimal tsunami inundation modeling strategy for large earthquakes in subduction zones. *Journal of Geophysical Research: Oceans*, *129*(9), e2024JC020941. doi: 10.1029/2024JC020941

Scala, A., Lorito, S., Romano, F., Murphy, S., Selva, J., Basili, R., … Cirella, A. (2020). Effect of Shallow Slip Amplification Uncertainty on Probabilistic Tsunami Hazard Analysis in Subduction Zones: Use of Long-Term Balanced Stochastic Slip Models. *Pure and Applied Geophysics*, *177*, 1497–1520. doi: 10.1007/s00024-019-02260-x

Schmedes, J., Archuleta, R. J., & Lavallée, D. (2010). Correlation of earthquake source parameters inferred from dynamic rupture simulations. *Journal of Geophysical Research: Solid Earth*, *115*(B3). doi: 10.1029/2009JB006689

Sementsov, K., & Nosov, M. (2023). Calculation of the Initial Elevation of the Water Surface at the Source of a Tsunami in a Basin with Arbitrary Bottom Topography. *Mathematical Models and Computer Simulations*, *15*(4), 746–758. doi: 10.1134/S2070048223040166

Sementsov, K. A., Baba, T., Kolesov, S. V., Tanioka, Y., & Nosov, M. A. (2024). The effect of earthquake fault rupture kinematics on tsunami generation: a numerical study of real events. *Geophysical Journal International*, *240*(2), 920–941. doi: 10.1093/gji/ggae413

Shaw, B. (2012). The ad 365 earthquake: Large tsunamigenic earthquakes in the hellenic trench. In *Active tectonics of the hellenic subduction zone* (pp. 7–28). Berlin, Heidelberg: Springer Berlin Heidelberg. doi: 10.1007/978-3-642-20804-1_2

Shaw, B., Ambraseys, N. N., England, P. C., Floyd, M. A., Gorman, G. J., Higham, T. F., … Piggott, M. D. (2008). Eastern Mediterranean tectonics and tsunami hazard inferred from the AD 365 earthquake. *Nature Geoscience 2008 1:4*, *1*, 268–276. doi: 10.1038/ngeo151

Shaw, B., & Jackson, J. (2010). Earthquake mechanisms and active tectonics of the Hellenic subduction zone. *Geophysical Journal International*, *181*, 966–984. doi: 10.1111/J.1365-246X.2010.04551.X

Shi, F., Kirby, J. T., Harris, J. C., Geiman, J. D., & Grilli, S. T. (2012). A high-order adaptive time-stepping TVD solver for Boussinesq modeling of breaking waves and coastal inundation. *Ocean Modelling*, *43-44*, 36–51. doi: https://doi.org/10.1016/j.ocemod.2011.12.004

Shi, Z., & Day, S. M. (2013). Rupture dynamics and ground motion from 3-d rough-fault simulations. *Journal of Geophysical Research: Solid Earth*, *118*(3), 1122–1141. doi: https://doi.org/10.1002/jgrb.50094

Simmetrix Inc. (2017). *SimModeler: Simulation Modeling Suite 11.0 Documentation, Tech. rep.*

Small, D. T., & Melgar, D. (2021). Geodetic coupling models as constraints on stochastic earthquake ruptures: An example application to PTHA in Cascadia. *Journal of Geophysical Research: Solid Earth*, *126*(7), e2020JB021149. doi: https://doi.org/10.1029/2020JB021149

Spratt, T. A. B. (1865). *Travels and Researches in Crete* (Vol. 2). J. van Voorst.

Stiros, S., & Drakos, A. (2006). A fault-model for the tsunami-associated, magnitude $\geq$ 8.5 Eastern Mediterranean, AD365 earthquake. *Z. Geomorphol*, *146*, 125–137.

Stiros, S. C. (2020). The AD 365 Ammianus tsunami in Alexandria, Egypt, and the Crete ca. 365 fault and tsunami. *Arabian Journal of Geosciences*, *13*(15), 716. doi: 10.1007/s12517-020-05667-2

Sørensen, M. B., Spada, M., Babeyko, A., Wiemer, S., & Grünthal, G. (2012). Probabilistic tsunami hazard in the Mediterranean Sea. *Journal of Geophysical Research: Solid Earth*, *117*. doi: 10.1029/2010JB008169

Tang, R., Zhu, S., & Gan, L. (2021). Dynamic rupture simulations of the 2008 7.9 wenchuan earthquake: Implication for heterogeneous initial stress and complex multifault geometry. *Journal of Geophysical Research: Solid Earth*, *126*(12), e2021JB022457. doi: https://doi.org/10.1029/2021JB022457

Tanioka, Y., & Satake, K. (1996). Tsunami generation by horizontal displacement of ocean bottom. *Geophysical Research Letters*, *23*(8), 861–864. doi: https://doi.org/10.1029/96GL00736

Taufiqurrahman, T., Gabriel, A.-A., Li, D., Ulrich, T., Li, B., Carena, S., ... Gallovič, F. (2023). Dynamics, interactions and delays of the 2019 Ridgecrest rupture sequence. *Nature*, *618*, 308–315. doi: 10.1038/s41586-023-05985-x

Taymaz, T., Jackson, J., & Westaway, R. (1990). Earthquake mechanisms in the Hellenic Trench near Crete. *Geophysical Journal International*, *102*(3), 695–731. doi: 10.1111/j.1365-246X.1990.tb04590.x

Tinti, E., Casarotti, E., Ulrich, T., Taufiqurrahman, T., Li, D., & Gabriel, A. A. (2021). Constraining families of dynamic models using geological, geodetic and strong ground motion data: The Mw 6.5, October 30th, 2016, Norcia earthquake, Italy. *Earth and Planetary Science Letters*, *576*, 117237. doi: 10.1016/J.EPSL.2021.117237

Tinti, S., Armigliato, A., Pagnoni, G., & Zaniboni, F. (2005). Scenarios of giant tsunamis of tectonic origin in the Mediterranean. *ISET Journal of Earthquake Technology, Paper No*, *464*, 171–188.

Titov, V., Kânoğlu, U., & Synolakis, C. (2016). Development of most for real-time tsunami forecasting. *Journal of Waterway, Port, Coastal, and Ocean Engineering*, *142*(6), 03116004. doi: 10.1061/(ASCE)WW.1943-5460.0000357

Titov, V. V., & Gonzalez, F. I. (1997). Implementation and testing of the method of splitting tsunami (most) model. *NOAA Technical Memorandum ERL PMEL-112*.

Triantafyllou, I., Agalos, A., Samaras, A. G., Karambas, T. V., & Papadopoulos, G. A. (2024). Strong earthquakes and tsunami potential in the hellenic subduction zone. *Journal of Geodynamics*, *159*, 102021. doi: 10.1016/j.jog.2024.102021

Ulrich, T., Gabriel, A.-A., Ampuero, J.-P., & Xu, W. (2019). Dynamic viability of the 2016 M_W 7.8 Kaikōura earthquake cascade on weak crustal faults. *Nature Communications 2019 10:1*, *10*, 1–16. doi: 10.1038/s41467-019-09125-w

Ulrich, T., Gabriel, A.-A., & Madden, E. H. (2021). GeoClaw input files of the 2004 Sumatra-Andaman tsunami scenarios published in Ulrich et al. (2021). *Zenodo*. doi: 10.5281/zenodo.5541510

Ulrich, T., Gabriel, A.-A., & Madden, E. H. (2022). Stress, rigidity and sediment strength control megathrust earthquake and tsunami dynamics. *Nature Geoscience*, *15*(1), 67–73. doi: 10.1038/s41561-021-00863-5

Ulrich, T., Vater, S., Madden, E. H., Behrens, J., van Dinther, Y., van Zelst, I., ... Gabriel, A.-A. (2019). Coupled, Physics-Based Modeling Reveals Earthquake Displacements are Critical to the 2018 Palu, Sulawesi Tsunami. *Pure and Applied Geophysics*, *176*, 4069–4109. doi: 10.1007/S00024-019-02290-5

Uphoff, C., Krenz, L., Ulrich, T., Wolf, S., Schneller, D., Kurapati, V., ... Bader, M. (2024). *SeisSol* [software]. doi: 10.5281/zenodo.4672483

Uphoff, C., Rettenberger, S., Bader, M., Madden, E. H., Ulrich, T., Wollherr, S., & Gabriel, A.-A. (2017). Extreme Scale Multi-Physics Simulations of the Tsunamigenic 2004 Sumatra Megathrust Earthquake. *Proceedings of the International Conference for High Performance Computing, Networking, Storage and Analysis SC17*. doi: 10.1145/3126908.3126948

Vallianatos, F., Michas, G., & Papadakis, G. (2014). Non-extensive and natural time analysis of seismicity before the mw6.4, october 12, 2013 earthquake in the south west segment of the hellenic arc. *Physica A: Statistical Mechanics and its Applications*, *414*, 163–173. doi: https://doi.org/10.1016/j.physa.2014.07.038

Vannucci, G., Pondrelli, S., Argnani, A., Morelli, A., Gasperini, P., & Boschi, E. (2004). An atlas of Mediterranean seismicity. *Annals of Geophysics*, *Suppl. to vol. 47*, 247 – 302.

Vernant, P., Reilinger, R., & McClusky, S. (2014). Geodetic evidence for low coupling on the Hellenic subduction plate interface. *Earth and Planetary Science Letters*, *385*, 122–129. doi: 10.1016/J.EPSL.2013.10.018

Volpe, M., Lorito, S., Selva, J., Tonini, R., Romano, F., & Brizuela, B. (2019). From regional to local SPTHA: efficient computation of probabilistic tsunami inundation maps addressing near-field sources. *Natural Hazards and Earth System Sciences*, *19*, 455–469. doi: 10.5194/nhess-19-455-2019

Vyas, J. C., Gabriel, A., Ulrich, T., Mai, P. M., & Ampuero, J. (2023). How does thermal pressurization of pore fluids affect 3D strike-slip earthquake dynamics and ground motions? *Bulletin of the Seismological Society of America*, *113*(5), 1992–2008. doi: 10.1785/0120220205

Wang, Y., Heidarzadeh, M., Satake, K., Mulia, I. E., & Yamada, M. (2020). A tsunami warning system based on offshore bottom pressure gauges and data assimilation for Crete Island in the Eastern Mediterranean Basin. *Journal of Geophysical Research: Solid Earth*, *125*(10), e2020JB020293. doi: 10.1029/2020JB020293

Wendt, J., Oglesby, D. D., & Geist, E. L. (2009). Tsunamis and splay fault dynamics. *Geophysical Research Letters*, *36*(15). doi: https://doi.org/10.1029/2009GL038295

Wilcox, L. C., Stadler, G., Burstedde, C., & Ghattas, O. (2010). A high-order discontinuous Galerkin method for wave propagation through coupled elastic–acoustic media. *Journal of Computational Physics*, *229*(24), 9373–9396. doi: https://doi.org/10.1016/j.jcp.2010.09.008

Williamson, A., Melgar, D., & Rim, D. (2019). The Effect of Earthquake Kinematics on Tsunami Propagation. *Journal of Geophysical Research: Solid Earth*, *124*(11), 11639–11650. doi: 10.1029/2019JB017522

Wilson, A., & Ma, S. (2021). Wedge plasticity and fully coupled simulations of dynamic rupture and tsunami in the Cascadia subduction zone. *Journal of Geophysical Research: Solid Earth*, *126*, e2020JB021627. doi: 10.1029/2020JB021627

Wirp, S. A., Gabriel, A. A., Schmeller, M., Madden, E. H., van Zelst, I., Krenz, L., ... Rannabauer, L. (2021). 3D Linked Subduction, Dynamic Rupture, Tsunami, and Inundation Modeling: Dynamic Effects of Supershear and Tsunami Earthquakes, Hypocenter Location, and Shallow Fault Slip. *Frontiers in Earth Science*, *9*, 177. doi: 10.3389/feart.2021.626844

Wirp, S. A., Gabriel, A.-A., Ulrich, T., & Lorito, S. (2024). Dynamic rupture modeling of large earthquake scenarios at the hellenic arc toward physics-based seismic and tsunami hazard assessment. *Journal of Geophysical Research: Solid Earth*, *129*(11), e2024JB029320. doi: https://doi.org/10.1029/2024JB029320

Withers, K. B., Olsen, K. B., Shi, Z., & Day, S. M. (2018). Validation of deterministic broadband ground motion and variability from dynamic rupture simulations of buried thrust earthquakes. *Bulletin of the Seismological Society of America*, *109*(1), 212–228. doi: 10.1785/0120180005

Wolf, S., Gabriel, A.-A., & Bader, M. (2020). Optimization and Local Time Stepping of an ADER-DG Scheme for Fully Anisotropic Wave Propagation in Complex Geometries. In V. V. Krzhizhanovskaya et al. (Eds.), *Computational science – iccs 2020* (pp. 32–45). Springer International Publishing.

Wollherr, S., Gabriel, A.-A., & Uphoff, C. (2018). Off-fault plasticity in three-dimensional dynamic rupture simulations using a modal Discontinuous Galerkin method on unstructured meshes: implementation, verification and application. *Geophysical Journal International*, *214*(3), 1556–1584. doi: 10.1093/gji/ggy213

Yamamoto, T. (1982). Gravity waves and acoustic waves generated by submarine earthquakes. *International Journal of Soil Dynamics and Earthquake Engineering*, *1*(2), 75–82. doi: 10.1016/0261-7277(82)90016-X

Yolsal, S., Taymaz, T., & Yalçiner, A. C. (2007). Understanding tsunamis, potential source regions and tsunami-prone mechanisms in the Eastern Mediterranean. *Geological Society Special Publication*, *291*, 201–230. doi: 10.1144/SP291.10

Yolsal-Çevikbilen, S., & Taymaz, T. (2012). Earthquake source parameters along the Hellenic subduction zone and numerical simulations of historical tsunamis in the Eastern Mediterranean. *Tectonophysics*, *536-537*, 61–100. doi: 10.1016/j.tecto.2012.02.019